Department of Physics and Astronomy

University of Heidelberg

Master thesis

in Physics

submitted by

Jonas Hörl

born in Herdecke

2018

Simulation of

ion-neutral merged beams experiments

at the Cryogenic Storage Ring

This Master thesis has been carried out by Jonas Hörl

at the

Max-Planck-Institut für Kernphysik

under the supervision of

Holger Kreckel

Simulationen zu Experimenten von Ionen- und Neutralstrahl Überlagerungen am kryogenen Speichering CSR:

Kollisionen zwischen Ionen und neutralen Teilchen sind die bestimmenden Reaktion für die Gasphasensynthese komplexer Moleküle in der interstellaren Materie (ISM). Um das astrochemische Netzwerk in ein Model zu fassen, werden Ratenkoeffizienten der vorhandenen Reaktionen benötigt. Diese wurden jedoch selten unter astophysikalischen Bedingungen gemessen. Der kryogene Speichering CSR am Max-Planck-Institut für Kernphysik ist in der Lage gespeicherte und gekühlte Ionen mit einem Strahl aus neutralen Atomen zu überlagern. Dabei können niedrige Kollisionsenergien bei sehr geringem Druck erzeugt werden. Um die Kollisionstemperatur abzuschätzen wurden Kollisionen zwischen H_3^+ und C simuliert, eine essenzielle Reaktion für die organische Astrochemie. Dazu wurde das Teilchen-Tracking Programm G4beamline benutzt, um den gespeicherten Ionenstrahl zu simulieren. Der neutrale Strahl wurde in einer ballistischen Näherung mit Python berechnet. Um den Einfluss des Erdmagnetfeldes auf den Ionenstrahl abzuschätzen, wurde es an über 400 Messpunkten um den Speicherring mit einem Fluxgate-Magnetometer aufgenommen. Eine Kompensation durch elektromagnetische Spulen wurde mit Finite-Elemente-Programm Opera 3D simuliert. Dabei konnte das Magnetfeld auf 1/10 gesenkt werden, wodurch Kollisionstemperaturen mit minimalen relativen Energien von 64 K ermöglicht werden können.

Simulation of ion-neutral merged beams experiments at the Cryogenic Storage Ring:

Collisions between ions and neutrals are decisive for the gas-phase synthesis of complex molecules in the interstellar medium. In order to model the astrochemical network, rate coefficients of existing reactions are required. However, these coefficients were barely measured under astrophysical conditions. The Cryogenic Storage Ring (CSR), housed by the Max Planck Institute for Nuclear Physics, is capable of merging stored and cooled ions with a neutral beam. This results in extremely low collision energies in a low pressure environment. In order to verify the collision temperatures, collisions between H_3^+ and C were simulated, a crucial reaction for organic astrochemisty. The particle tracking program G4beamline was used to simulate the stored ion beam. The neutral beam was calculated by python in a ballistics approach. The influence of the earth's magnetic field was evaluated by recording the magnetic field with a fluxgate magnetometer at over 400 measuring points. The compensation of the earth's magnetic field by electromagnetic coils was simulated by the finite element program Opera-3D. Thus, the magnetic field inside the CSR could be reduced to 1/10 of its former power, enabling collision temperatures down to 64 K.

Contents

1 Introduction

The interstellar medium (ISM) is the matter between the star systems in a galaxy. It consists mainly of hydrogen and helium and has a average density of $\sim 1\ \mathrm{cm}^{-3}$. Regions of high concentrations of gas and dust particles are called interstellar clouds. A molecular cloud is a type of interstellar cloud, where the density, temperature and size permits the formation of molecules. Cloud densities and temperatures range from 10 cm^{-3} to 10^6 cm^{-3} and from 10 K to 100 K, respectively. Despite these extreme conditions, almost 200 molecules have been detected in the ISM [1]. The population of these species is determined by the formation and the destruction processes. Due to the low density in interstellar clouds, three-body reactions are unlikely and two-body reactions dominate. Although neutral species are most abundant, neutral-neutral reactions are often suppressed owing to the presence of activations barriers and the lack of attractive forces between the reactants. Anion-cation reactions are energetically favourable, but infrequent due to the low abundance of negative ions in the ISM. Thus, exothermic ion-neutral reactions dominate in the interstellar gas-phase and are the key formation reactions.
Vast amount of data has been gathered from various space telescopes, Herschel [2] and Spitzer [3], and the new generation, the airborne observatory SOFIA [4] and the astronomical interferometer ALMA [5]. In order to evaluate the information gained from astronomical observations, laboratory studies and models of the interstellar chemical network are needed. In 1973, a pioneering work about chemistry in interstellar clouds was published [6]. By this time, most rate coefficients were measured using flowing afterglows [7]. In this technique an ionized carrier gas, normally helium, is introduced at one end of a tube and exhausted at the other end. By injecting a neutral gas into the tube it can react with He^+, producing positive ions. Rate measurements of the mass-selected daughter products lead directly to a reaction rate coefficients. Selected ion flow tube (SIFT) technique refined this method, removing the carrier gas before reaction [8]. Investigating ion-neutral collisions, virtually no other techniques have been used. As a consequence most rate coefficients were measured at room temperature and at relatively high pressures, in

contrast to the astrophysical conditions of the models they are used in.
This work describes an experiment capable of investing gas-phase reactions at astrophysical relevant temperatures: the merged beams experiment at the Cryogenic Storage Ring (CSR) at the Max Planck Institute for Nuclear Physics. Both collision partners have to be produced in defined states before the experiment. The molecular ions are created in suitable ion sources and stored in the cryogenic environment of the CSR for cooling, while the ground term neutral atoms are produced by photodetachment of negative ions.
After introducing the principles of ion beam transport via electromagnetic fields, phase ellipses are discussed, as a way to describe an ion beam as a whole. Subsequently, a brief overview is presented over the CSR and the incorporated merged beams experiment, where a cooled ion beam and a a well-defined neutral atomic beam superpose. Afterwards, details are offered on the simulation of the merged beams experiment, using the example of reactions between H_3^+ and neutral C atoms. The results are described thereafter, estimating the collision temperatures in dependence of an external magnetic field, the beam emittance and the velocity match between the beams. A series of measurements containing over 400 data points around the storage ring evaluates the influence of the earth's magnetic field on the ion beam. After presenting a configuration of electromagnetic coils compensating the earth's magnetic field, the expected improvement on the merged beams experiment is estimated. Eventually, the results are summarized and perspectives are given.

2 Principles of ion beam transport

2.1 Deflection and Acceleration Forces on Particles

The interaction between the electromagnetic field and charged particles depends on the forces deflecting, focusing and accelerating it. The central equation in accelerator physics is known as Lorentz force

$$\mathbf{F} = q\left(\mathbf{E} + \mathbf{v} \times \mathbf{B}\right), \tag{2.1}$$

where q is the charge, $\mathbf{v}$ is the velocity of the charged particle, $\mathbf{E}$ is the electrical field, $\mathbf{B}$ is the magnetic field and $\times$ the vector cross product. Field intensities of $\mathbf{E}$ and $\mathbf{B}$ depend on space $\mathbf{r}$ and time t. The Lorentz force is invariant when performing a Lorentz transformation. Single charged particles have a charge equal to the elementary charge $q = e$. The charge of heavy ions depends on the state of ionisation. The charge is equal to the nuclear charge $q = \mathrm{Z}e$ if all electrons are removed from the electron shell.

Forces acting perpendicular to the particle's velocity $\mathbf{v}$ produce circular deflections. Thus, neither does the absolute velocity $|\mathbf{v}|$ change nor does the kinetic energy. Forces acting parallel to the particles velocity $\mathbf{v}$ leading to a change of the absolute velocity $|\mathbf{v}|$, hence to change of the kinetic energy. $\mathbf{B}$ fields generate forces perpendicular the particle's velocity $\mathbf{v}$ and therefore are only used for deflection and focusing. Acceleration in the sense that the kinetic energy changes can only be achieved with $\mathbf{E}$ fields.

A change in the particle momentum can be obtained from the time integral

$$\Delta\mathbf{p} = \mathbf{p}\left(t_2\right) - \mathbf{p}\left(t_1\right) = \int_{t_1}^{t_2} \mathbf{F}\mathrm{d}t. \tag{2.2}$$

A change in kinetic energy between position $\mathbf{r}_1$ and $\mathbf{r}_2$ can be obtained from the line integral

$$\Delta E = E\left(\mathbf{r}_2\right) - E\left(\mathbf{r}_1\right) = \int_{\mathbf{r}_1}^{\mathbf{r}_2} \mathbf{F}\mathrm{d}r. \tag{2.3}$$

Since $\mathrm{d}r$ is perpendicular to $\mathbf{v} \times \mathbf{B}$, $(\mathbf{v} \times \mathbf{B})\mathrm{d}r = 0$ is valid and

$$\Delta E = \int_{\mathbf{r}_1}^{\mathbf{r}_2} q\,(\mathbf{E} + \mathbf{v} \times \mathbf{B})\,\mathrm{d}r = \int_{\mathbf{r}_1}^{\mathbf{r}_2} q\mathbf{E}\mathrm{d}r, \tag{2.4}$$

meaning only the electric field $\mathbf{E}$ contributes to the change in energy, to be exact only the component $\mathbf{E}_{||}$ parallel to the particles velocity $\mathbf{v}$. Solving for the component $\mathrm{d}\mathbf{p}_{||}/\mathrm{d}t$ parallel to $\mathbf{v}$

$$q\mathbf{E}_{||} = \frac{\mathrm{d}\mathbf{p}_{||}}{\mathrm{d}t} = m\frac{\mathrm{d}\mathbf{v}_{||}}{\mathrm{d}t}. \tag{2.5}$$

The component $\mathbf{E}_{\perp}$ perpendicular to $\mathbf{v}$ causes merely a change in direction in the same way as $(\mathbf{v} \times \mathbf{B})$ does,

$$q\,(\mathbf{E}_{\perp} + \mathbf{v} \times \mathbf{B}) = \frac{\mathrm{d}\mathbf{p}_{\perp}}{\mathrm{d}t} = m\frac{\mathrm{d}\mathbf{v}_{\perp}}{\mathrm{d}t}. \tag{2.6}$$

Radial acceleration $\mathrm{d}\mathbf{v}_{\perp}/\mathrm{d}t$ leads to circular deflection. The centripetal force yields the current radius of curvature ρ

$$\left|\frac{\mathrm{d}\mathbf{v}_{\perp}}{\mathrm{d}t}\right| = \frac{v^2}{\rho}. \tag{2.7}$$

Although space charge effects were neglected in simulations later on, they should not be left unmentioned. In this process, the acting forces do not arouse from external **E**- and **B**-fields, but from the electromagnetic interaction between the charged particles of the beam. The magnitude is determined by particle density of the beam. Its impact is the most with a high amount of space charge and a low velocity of the particles. Particles trajectories diverge due to repulsive coulomb forces caused by the space charge effects, leading to continuous defocusing of the beam and a steady increase of the emittance.

2.2 Motion of Particles in Linear Approximation

An ion beam consists of a large number of charged particles. In the case of storage rings it is desired to direct the beams path. This is done by ion-optical elements creating electromagnetic fields. The force acting on charged particles in an electromagnetic field is given by the Lorentz force (Eq. 2.1). From Eq. 2.1, the equations of motion can be derived for a charged particle, moving in an electromagnetic field.

Here the equations of motion of a charged particle are derived solely due to the influence of the magnetic field. The derivation of the motion of a particle in an electric field can be determined in the same manner. The motion of a particle affected due to a magnetic field is given as

$$\mathbf{F} = \dot{\mathbf{p}} = q\mathbf{v} \times \mathbf{B}. \tag{2.8}$$

An ion beam takes a circular path through a magnetic deflector. It is specified through the radius of curvature ρ_0. The orthogonal (x, y) coordinate system moves along the central path and has a velocity v_s equal to the projection of the particle velocity to the central path. If a particle is displaced by a small amount x in x-direction relative to the central path, the new curvature, induced by the magnetic field, can be described by the radius $(\rho_0 + x)$. The centrifugal force F_C acting on this particle can be derived by

$$F_C = \frac{m v_s^2}{\rho_2 + x}, \tag{2.9}$$

where m represents the particle mass and $v_s \approx v_z$ the linearly approximated velocity. The particles motion in the moving (x, y) coordinate system an be rewritten using Eq. 2.8 and Eq. 2.9, leading to

$$\begin{aligned} \ddot{x} &= \frac{q}{m}\left(v_y B_z - v_z B_y\right) + \frac{v_s^2}{\rho_0 + x}, \\ \ddot{y} &= \frac{q}{m}\left(v_z B_x - v_x B_z\right). \end{aligned} \tag{2.10}$$

With the linear approximation $v_s \approx v_z$ Eq. 2.10 can be simplified to

$$\begin{aligned} \ddot{x} &= -\frac{q}{p} v_s^2 B_y + \frac{v_s^2}{\rho_0 + x}, \\ \ddot{y} &= \frac{q}{p} v_s^2 B_x, \end{aligned} \tag{2.11}$$

where p describes the total momentum of the particle. Using a series expansion on Eq. 2.11, the first order terms are

$$\begin{aligned} \ddot{x} &= -\frac{q}{p} v_s^2 B_y + \frac{v_s^2}{\rho_0}\left(1 - \frac{x}{\rho_0}\right), \\ \ddot{y} &= \frac{q}{p} v_s^2 B_x. \end{aligned} \tag{2.12}$$

With the relations

$$\begin{aligned} \frac{\mathrm{d}}{\mathrm{d}t} &= \frac{\mathrm{d}s}{\mathrm{d}t}\frac{\mathrm{d}}{\mathrm{d}s} = v_s\frac{\mathrm{d}}{\mathrm{d}s}, \\ \frac{\mathrm{d}^2}{\mathrm{d}t^2} &= v_2^2\frac{\mathrm{d}^2}{\mathrm{d}s^2}, \end{aligned} \tag{2.13}$$

the equation of motion Eq. 2.12 can be rewritten,

$$\begin{aligned} x'' &= -\frac{q}{p}B_y + \frac{1}{\rho_0}\left(1 - \frac{x}{\rho_0}\right), \\ y'' &= \frac{q}{p}B_x. \end{aligned} \tag{2.14}$$

The magnetic field term can be expanded as long as the particle trajectory demonstrated only small deviations to the central path

$$\begin{aligned} B_y(x) &= B_0 + \frac{\partial B_y}{\partial x}x + \frac{1}{2!}\frac{\partial^2 B_y}{\partial x^2}x^2 \cdots, \\ B_x(y) &= 0 + \frac{\partial B_x}{\partial y}y + \frac{1}{2!}\frac{\partial^2 B_x}{\partial y^2}y^2 \cdots. \end{aligned} \tag{2.15}$$

In linear approximation of Eq. 2.15 and with $p_0 = qB_0\rho_0$, Eq. 2.14 can be rewritten as

$$\begin{aligned} x'' &= -\left(\frac{q}{p}\frac{\partial B_y}{\partial x} + \frac{1}{\rho_0^2}\right)x, \\ y'' &= \frac{q}{p}\frac{\partial B_x}{\partial y}y. \end{aligned} \tag{2.16}$$

Taking into account the momentum deviation $\delta = \Delta p/p_0$ to the central particle with the momentum p_0 and substituting $k_x = \frac{q}{p}\frac{\partial B_y}{\partial x} + \frac{1}{\rho_0^2}$ and $k_y = -\frac{q}{p}\frac{\partial B_x}{\partial y}$, respectively, leads to the final form

$$\boxed{\begin{aligned} x'' + k_x x &= \frac{\delta}{\rho_0}, \\ y'' + k_y y &= 0. \end{aligned}} \tag{2.17}$$

2.3 Solution of Linear Equation of Motion

General Solution

In the case of mono-energetic particles ($\delta = 0$), the equations of motion (Eq. 2.17) both have the same structure, which is given by

$$\boxed{u'' + ku = 0.} \tag{2.18}$$

A general solution of such a differential equation can always be given by a pair of linear independent distinctive solutions $C(s)$ and $S(s)$:

$$\begin{aligned} u(s) &= u_0 C(s) + u_0' S(s), \\ u'(s) &= u_0 C'(s) + u_0' S'(s), \end{aligned} \tag{2.19}$$

where u_0 and u_0' are the initial parameters. They indicate the deviation in space and direction at the starting point. The functions $C(s)$ and $S(s)$ are called cosine-like or sine-like and satisfy the following conditions:

$$\begin{aligned} C(0) &= 1, \quad C'(0) = 0, \\ S(0) &= 0, \quad S'(0) = 0. \end{aligned} \tag{2.20}$$

If the particles are not mono-energetic ($\delta \neq 0$), the differential equation becomes inhomogeneous (see Eq. 2.17) for deviations in radial positions close to an ion-optical element which deflects the particle. A general solution can be given as a linear combination of the homogeneous solution (Eq. 2.19) and a particular solution of the inhomogeneous equation $\delta d_x(s)$. $d_x(s)$ describes the dispersion function [9] which must satisfy the initial conditions:

$$d_x(0) = 0, \quad d_x'(0) = 0. \tag{2.21}$$

Characteristic Solutions

Using the linear approximation, the most relevant ion-optical elements are drift sections without a field ($k = 0$), quadrupole magnets, deflection electrodes and magnets. Assuming that k is constant within an ion-optical element Eq. 2.18 can be identified with the differential equation of a harmonic oscillator. The traversal motion of particles within ion-optical elements ($0 \leq s \leq L$) is given by the characteristic

solutions [9]:

- For $K(s) > 0$ (focusing):

$$\begin{aligned} C(s) &= \cos\left(\sqrt{k}s\right), \\ S(s) &= \frac{1}{\sqrt{k}} \sin\left(\sqrt{k}s\right), \\ d_x(s) &= \frac{1}{\rho_0 k}\left[1 - \cos\left(\sqrt{k}s\right)\right]. \end{aligned} \tag{2.22}$$

- For $K(s) = 0$:

$$\begin{aligned} C(s) &= 1, \\ S(s) &= s, \\ d_x(s) &= 0. \end{aligned} \tag{2.23}$$

- For $K(s) < 0$ (defocusing):

$$\begin{aligned} C(s) &= \cosh\left(\sqrt{|k|}s\right), \\ S(s) &= \frac{1}{\sqrt{|k|}} \sinh\left(\sqrt{|k|}s\right), \\ d_x(s) &= \frac{1}{\rho_0 |k|}\left[\cosh\left(\sqrt{|k|}s\right) - 1\right]. \end{aligned} \tag{2.24}$$

The variation in the longitudinal displacement l between the particle of interest and a reference particle at the central path is given by $l = -v_0(t - t_0)$. t and t_0 denote the time of flight between two planes for the particle of interest and the reference particle, respectively. Longitudinal displacements solely appear due to deflecting ion-optical elements since the path length can differ. Longitudinal displacement can be neglected while using continuous ion beams and is only of interest in combination with bunched beams.

Phase Ellipse

An ion beam is formed by a superposition of several particle trajectories. Since determining every single trajectory becomes impractical as the particle number rises, looking at the whole beam becomes very appealing. The phase space density $\rho\left(x, x', y, y', l, \delta\right)$ is able to fully characterise an ion beam. Assuming that the

horizontal (x, x'), vertical (y, y') and longitudinal (l, δ) coordinates are not correlated, the phase space density can be split into two-dimensional distributions: $\rho(x, x', y, y', l, \delta) = \rho(x, x')\,\rho(y, y')\,\rho(l, \delta)$. Usually these distributions can be edged by an ellipse, which provides the general properties of the particle beam.
The horizontal phase ellipse should serve as an example. Phase space ellipses can be represented by a symmetric 2×2-matrix with a positive determinant, the so-called σ-matrix [10]:

$$\sigma_x = \begin{pmatrix} \sigma_{11} & \sigma_{12} \\ \sigma_{21} & \sigma_{22} \end{pmatrix} = \begin{pmatrix} \sigma_{11} & \sigma_{12} \\ \sigma_{12} & \sigma_{22} \end{pmatrix}. \tag{2.25}$$

The equation of the phase ellipse is given by

$$\boxed{\boldsymbol{X}^T \sigma_x^{-1} \boldsymbol{X} = 1,} \tag{2.26}$$

where $\boldsymbol{X}$ denotes the vector from the origin of coordinates to a point on the ellipse,

$$\boldsymbol{X}^T = (x, x'), \quad \boldsymbol{X} = \begin{pmatrix} x \\ x' \end{pmatrix}. \tag{2.27}$$

The inverse matrix σ_x^{-1} is determined by

$$\sigma_x^{-1} = \frac{1}{det\,(\sigma_x)} \begin{pmatrix} \sigma_{22} & -\sigma_{12} \\ -\sigma_{12} & \sigma_{11} \end{pmatrix}. \tag{2.28}$$

Solving Eq. 2.26 leads to an equation for the phase ellipse

$$\sigma_{22} x^2 - 2\sigma_{12} x x' + \sigma_{11} x'^2 = \det(\sigma_x) = \epsilon_x^2, \tag{2.29}$$

where ϵ_x indicates the emittance. The value of ϵ_x times π defines the area E_x of the phase space ellipse

$$E_x = \pi \epsilon_x = \pi \sqrt{\det \sigma_x} = \pi \sqrt{\sigma_{11}\sigma_{22} - \sigma_{12}^2}. \tag{2.30}$$

Assuming that the density distribution $\rho(x, x')$ of the area encircled by the phase space ellipse is normally distributed

$$\rho(\boldsymbol{x}) = \frac{1}{2\pi\epsilon_x} exp\left(-\frac{1}{2}\boldsymbol{x}^T \sigma_x^{-1} \boldsymbol{x}\right), \tag{2.31}$$

where **x** denotes arbitrary phase space coordinates. The density distribution can be represented by elliptical contour lines. The phase ellipse

$$\boldsymbol{X}^T \sigma_x^{-1} \boldsymbol{X} = 1 \tag{2.32}$$

marks the contour line where the density is lowered by a factor of $exp(-1/2)$ compared to the center. This corresponds to one standard deviation at the beam profile and hence encloses $39,3\%$ of the total intensity. The value for the beam emittance depends on the chosen phase ellipse. Therefore the fraction of included particles has to be indicated. This can be done in standard deviations or percent.
Rewriting Eq. 2.25 using the twiss parameters α, β and γ [10] yields

$$\sigma = \epsilon \begin{pmatrix} \beta & -\alpha \\ -\alpha & \gamma \end{pmatrix}. \tag{2.33}$$

The betatron function $\beta_x(s)$ is correlated to the maximum beam radius $x_{max}(s)$ as followed

$$x_{max}(s) = \sqrt{\epsilon_x \beta_x(s)}. \tag{2.34}$$

The parameter $\alpha(s)$ is represented by the derivative of $\beta(s)$,

$$\alpha(s) = -\frac{\beta'(s)}{2}. \tag{2.35}$$

The last twiss parameter γ is defined as

$$\gamma = \frac{1+\alpha^2}{\beta}. \tag{2.36}$$

This twiss parameter γ and the beam emittance ϵ provide the the maximum divergence x'_{max}

$$x'_{max} = \sqrt{\epsilon_x \gamma_x}. \tag{2.37}$$

As the twiss parameters are independent of the phase space area, they describe the ion beam transport conveniently.

3 Basic Theory of Ion-Neutral Collisions

The interstellar medium (ISM) is mainly made up of atoms and molecules. Most of the detected molecules in space are formed by gas-phase processes. Moreover, they appear to be dominated by ion-molecule reactions. Another important route of molecule formation, not being limited to ion-neutral collision partners, occurs on the surface of dust grains. Knowing the rate coefficients of these reactions is crucial for evaluate their role in astrochemistry. With databases containing more than 4000 reactions, the abundance of many of the ∼180 yet detected molecules in the ISM could be predicted by chemical models.

In order to set up chemical models it is important to know the reaction rates in great detail. Particularly their temperature dependency and their branching ratios in the case of reactions with different product channels. Additionally, information about the initial temperature and initial abundances plays a significant role. However, only a fraction of the relevant reactions are characterized in the laboratory. Moreover, rarely the temperature dependence was measured, which can generally be stated in the Arrhenius-Kooij formula [11]

$$k(T) = \alpha(T/300K)^{\beta} \exp\left(\frac{-\gamma}{T}\right), \tag{3.1}$$

where the parameter α describes the overall size of the rate coefficient, while β and γ characterize its temperature dependence. Only for reactions hindered by a barrier or endothermicity γ is unequal to zero. While the important H_3^+ forming reaction $H_2^+ + H_2 \rightarrow H_3^+ + H$ does not show a temperature dependence at all, generally reactions of ions with molecules show a reverse temperature dependence. In other words, the rate coefficient increases at lower temperatures.

As proposed by F. Lindemann [12] ion-molecular reactions can be broke down into two elementary steps. According to this model, an intermediate molecular complex is formed through a collision. In order to release the excited energy, the intermediate molecular collisions complex need to interact with a third body or emit a photon.

Picking the example of $C^+ + H_2$ reacting to CH_2^+ the two-step association process

can be written as

$$C^+ + H_2 \underset{k_2}{\overset{k_1}{\rightleftharpoons}} (C + H_2)^{+^*} \xrightarrow{k_3} (C H_2)^+ + h\,\nu, \tag{3.2}$$

where C^+ and H_2 fill the role of the colliding ion-molecule pair and k_1, k_2 and k_3 represent the reaction rate constants for combination, decomposition and radiative stabilization. $h\nu$ describes the radiation and $(C + H_2)^{+^*}$ the intermediate complex with a characteristic lifetime $\tau_2 = 1/k_2$, against decomposition back to reactants C^+ and H_2. The lifetime τ_2 is strongly temperature dependent, increasing up to microseconds in cold molecular clouds. Compared to that, the radiative lifetime $\tau_3 = 1/k_3$, describing the process stabilizing by emitting a photon, is rather long being in the order of milliseconds. Thus, the chances to form CH_2^+ are rather small and temperature dependent because the decomposition lifetime τ_2 plays a determinative role. However, regardless of the reaction conditions, this reaction is a dominant pathway to form carbonaceous species in space.
On the contrary, reactions with a slow decomposition process k_2 and a fast radiative stabilization process k_3 are generally limited by the combination rate k_1. In this case, the Langevin collision theory [13] presents a good estimate of the rate coefficient. Generally a two-body rate coefficient $k(E)$ at a given energy E is given by

$$k(E) = v\sigma(E), \tag{3.3}$$

where v describes the relative velocity of the collision partners and is proportional to $\sqrt{E}$, where E is the kinetic energy of the collision in the center-of-mass frame. Similar to a hard sphere model, the capture collision section is defined as [13]:

$$\sigma(E) = \pi b_c^2. \tag{3.4}$$

The impact parameter b describes the closest distance between a potential field center and a projectile if it were not deflected. Fig. 3.1 illustrates a ion-neutral collision with the impact parameter b, where the attractive force originates from an induced dipole moment in the neutral collision partner. b_c describes a critical value of the impact parameter b, where the angular momentum barrier can be surmounted, thus enabling collisions.
The Langevin theory describes the effective potential between neutral atom or

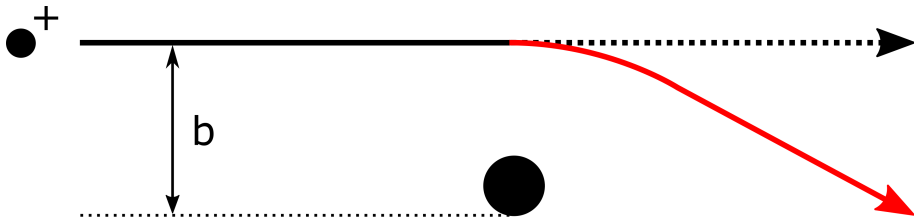

Figure 3.1: Schematic depiction of the impact parameter b for a collision between a neutral molecule or atom (large sphere) and an ion (small sphere). The ion induces a dipole moment on the neutral particle and subsequently gets deflected.

molecule and an ion inducing a dipole on the former one:

$$V_{eff}(r) = -\frac{1}{8\pi\epsilon_0}\frac{q^2 \cdot a_n}{r^4} + E \cdot \left(\frac{b}{r}\right)^2, \tag{3.5}$$

where q denotes the ions charge, a_n represents the polarizability of the neutral collision partner, r is the distance between them and $\epsilon_0 = 8,85\frac{As}{Vm}$ is the vacuum permittivity. The first term gives rise to the attractive ion induced dipole force, while the second one depicts the centrifugal potential yielding repulsive forces. From the conditions $\delta V_{eff}/\delta r = 0$ and $\delta V_{eff} = E(r)$ the maximum critical impact parameter, where the centrifugal potential barrier can be surmounted, can be found

$$b_c^2 = \sqrt{\frac{q^2 a_n}{2\pi\epsilon_0 E}}. \tag{3.6}$$

Inserting the critical impact parameter in Eq. 3.4 imposes a proportionality $\sigma(E) \propto E^{-\frac{1}{2}} \propto 1/v$ and finally yields the temperature independent Langevin value as described by Giomousis and Stevenson [13]

$$k_L = q\sqrt{\frac{\pi a_n}{\epsilon_0 \mu}}, \tag{3.7}$$

where μ denotes the reduced mass. In the case of ion-molecule reactions this model mostly describes an upper limit for the rate coefficients. Since especially collision restrictions as barriers or endothermicity may cause deviations, the rate coefficient of exothermic ion-neutral reactions shows a relative smooth behaviour without any sharp resonances. For some cases, where the chemical attraction is stronger than predicted by this model, rate coefficients also can exceed the Langevin value. This is

the case for the reaction $H^- + H$. In the end, the Langevin value provides a proper assessment in order to distinguish between fast and slow reactions.

4 The Cryogenic Storage Ring (CSR)

The Cryogenic Storage Ring (CSR) is a storage ring capable of storing beams of anions and cations at kinetic energies between 20 and 300 keV per charge unit. In order to be able to investigate large molecules and clusters, only electrostatic elements are used inside the CSR. Thus, charged particles can be stored independent of their mass. A closed-cycle helium system ensures that the experimental vacuum chamber, housing the stored beam with all its beam optics, can be cooled down below 10 K. Coper sheets wrapping the experimental vacuum chamber are connected

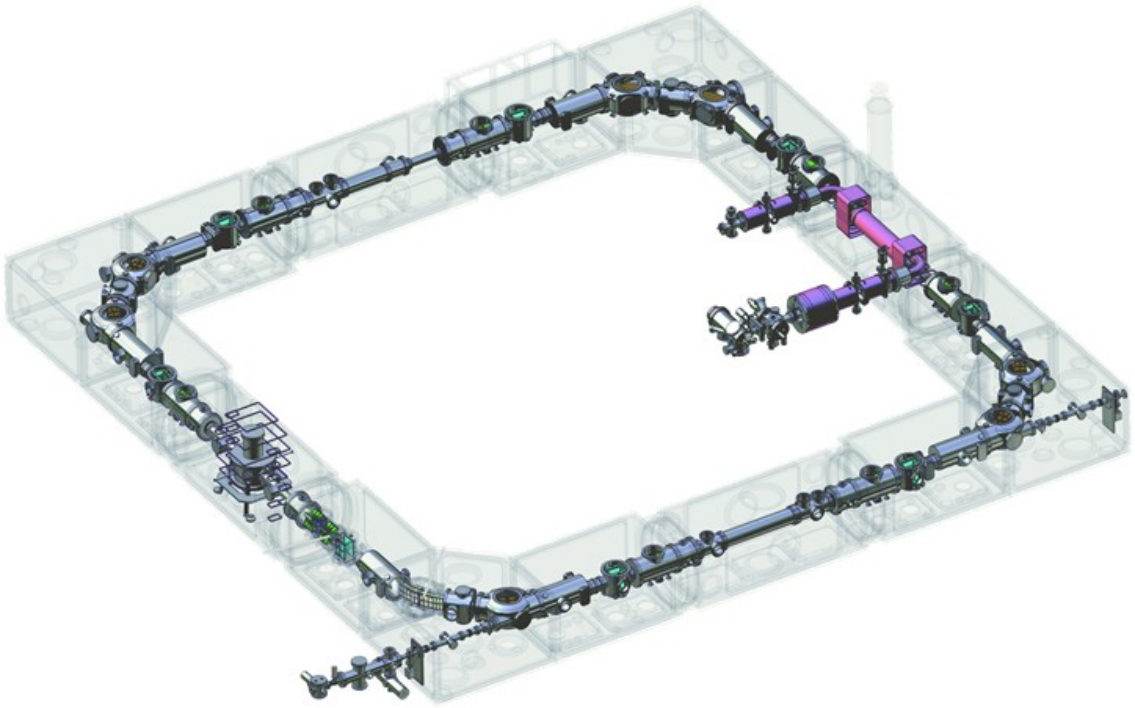

Figure 4.1: Schematic depiction of the CSR. Ion and neutral beams can be injected in the bottom corner. After crossing the first straight section ion-neutral reaction products can leave the ring, being detected afterwards. Anticlockwise, the second straight section houses the electron cooler indicated in purple colour. The third section is dedicated to beam diagnostics and the last one provides space for the future installation of a reaction microscope.

via copper cables to the 2 K He line, enabling temperature transfer due to their high thermal conductivity. The experimental vacuum chamber is surrounded by an isolation vacuum chamber ($< 10^{-5}$ mbar), which houses a 40 K and 80 K radiation shield. While the 40 K shield surrounds the inner vacuum chamber, the 80 K envelopes the 40 K shield. A 5 K helium line is recirculated four times all around the ring to cool the cryogenic equipment and subsequently the two radiation shields at 40 K and 80 K. While the bottom plates of the 40 K radiation shield carry the vacuum chamber, all the ion optical elements of the CSR are mostly mechanically decoupled from the experimental vacuum chamber by mounting them individually on external concrete support blocks. Moreover, care was taken to only use non magnetic components. This way the earth's external magnetic field will not be enhanced by perturbations at the beam position.
In order to achieve residual gas densities below 140 cm^{-3} (corresponding to a room temperature pressure of 10^{-14} mbar), first the vacuum chambers are baked out at $\sim$250 °C to remove volatile compounds. Turbomolecular pumps in conjunction with ion getter pumps, which bind the residual gas molecules, attain pressures of $\sim 10^{-11}$ mbar in the experimental vacuum chamber. Cooling down the entire inner vacuum chambers below 10 K yields the desired gas density as most chemical elements condensate on the chamber surface. As a result, measured lifetimes ranges from a few hundred seconds up to almost an hour. The cold environment as well as the long storage time allow stored molecules to radiatively cool into their rovibartional ground states.

4.1 The Ring Lattice

The CSR lattice consists of electrostatic ion-optical elements, namely cylindrical deflectors and quadrupole doublets. At the corners, the 90° bend is split up in two 6°-deflectors and two 39°-deflectors. On the one hand the 1.1 m distance between the 6°- and 39°-deflector enables the injection of an ion or neutral beam. On the other hand it provides the space to detect neutral fragments which are generated in experiments. During the injection of an ion beam one 6°-deflector is switched to ground. This way the ion beam does not get deflected and can enter the storage ring. After one circuit the 6°-deflector has to be switched back to storing voltage in order to properly store the ion beam.
The focusing quadrupoles have a length of 0.2 m and are separated by 0.15 m within a

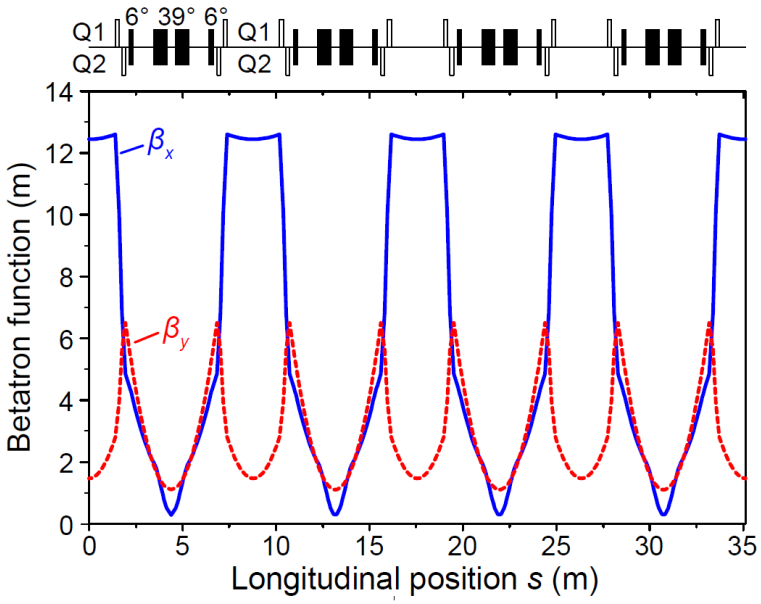

Figure 4.2: Simulated horizontal and vertical betatron functions β_x (solid blue line) and β_y (red dashed line) for the standard operating mode of the CSR, adopted from [14].

doublet. The gap between the quadrupole doublets offers space for experiments. The first straight section after the injection houses ion-neutral reaction measurements. Here the stored ion beam can be superimposed by a neutral atom beam and cross sections are calculated by the means of their the daughter products. Following anticlockwise, the second straight section permits the addition of a collinear merged electron beam for electron collision studies and phase-space cooling to a wide range of stored ion species [15]. The stored ion beam cools due to a merger with a velocity-matched electron beam, which is geometrical well defined and has a narrow energy distribution. The third section focuses on beam diagnostics. It relies on three different pick-up modules [16, 17] and a beam viewer [18]. The fourth section is currently under development. It is planned to install a reaction microscope [19], which allows the investigation of collision processes, using Cold Target Recoil Ion Momentum Spectroscopy (COLTRIMS) [20].

The storage ring can be described by a closed periodic system. The transfer matrices program Methodical Accelerator Design (MAD8) [21] was used to simulate CSR lattice in linear approximation [14]. Fig. 4.2 shows the horizontal (x) and vertical (y) betatron functions β_x and β_y, starting at the center of a straight CSR section. For the starting position the Twiss parameters were calculated: $\alpha_x = \alpha_y = 0$,

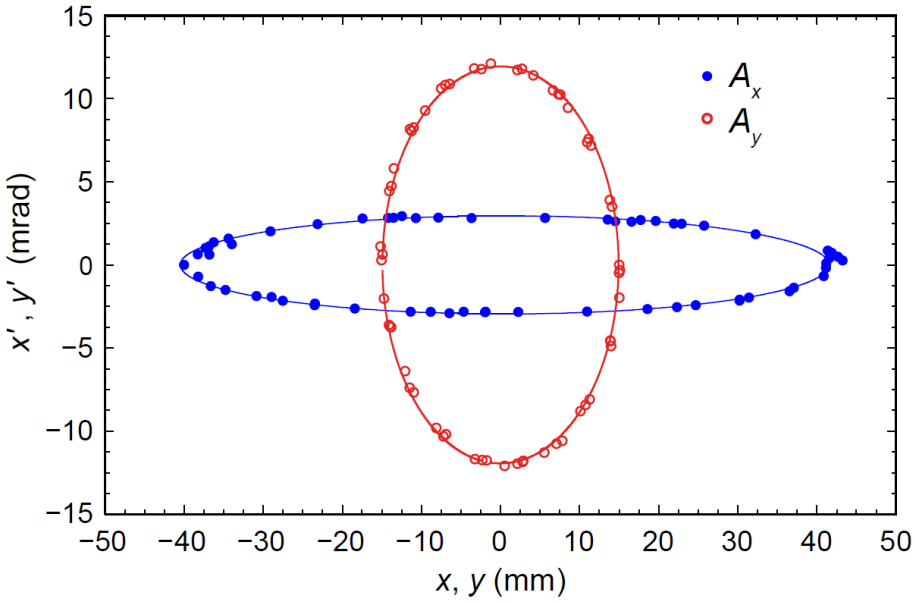

Figure 4.3: Opera-3d simulation of a single particle, showing its the phase space. It started at the center of a straight section of the CSR with x = 40 mm, y = 15 mm and x' = y' = 0. The transverse positions and angles on subsequent turns at the same longitudinal position are indicated with dots, forming a phase space ellipse. The maximum phase space for a stable ion storage defines a ring acceptance. The maximum horizontal and vertical beam sizes at this position are found to be ±40 mm and ±15 mm respectively. Leading to the acceptances A_x = 180 mm mrad and A_y = 120 mm mrad.[14].

$\beta_x = 12.3$ m and $\beta_y = 1.2$ m. In the case of a ring lattice the Twiss parameters are called machine parameters. The injected beam has to match these parameters in order to be stored stably.

The ring acceptance is defined as the maximum beam emittance that can be stored. It is primarily limited by the field quality of the quadrupoles. Since MAD 8 only considers linear ion-optical effects, the finite element program Opera-3d [22] was used to calculate the acceptance. Fig. 4.3 shows the maximum phase space ellipses at the center of a straight CSR section, yielding to the horizontal A_y = 120 mm mrad and the vertical acceptance A_x = 180 mm mrad.

4.2 The Merged Beams Experiment

As mentioned in chapter 4.1, the first straight section of the CSR is dedicated for measurements of ion-neutral reactions. The goal is to investigate cross-sections of ion-neutral reactions under astrophysical conditions. This is achieved by merging the ion beam, stored in the CSR, with a neutral atom beam. The cross sections are calculated with the aid of their the daughter products. Fig 4.4 shows a schematic overview of the CSR transfer line. Particles injected into the CSR may be generated at two different ion sources employing two different electrostatic platforms, designed

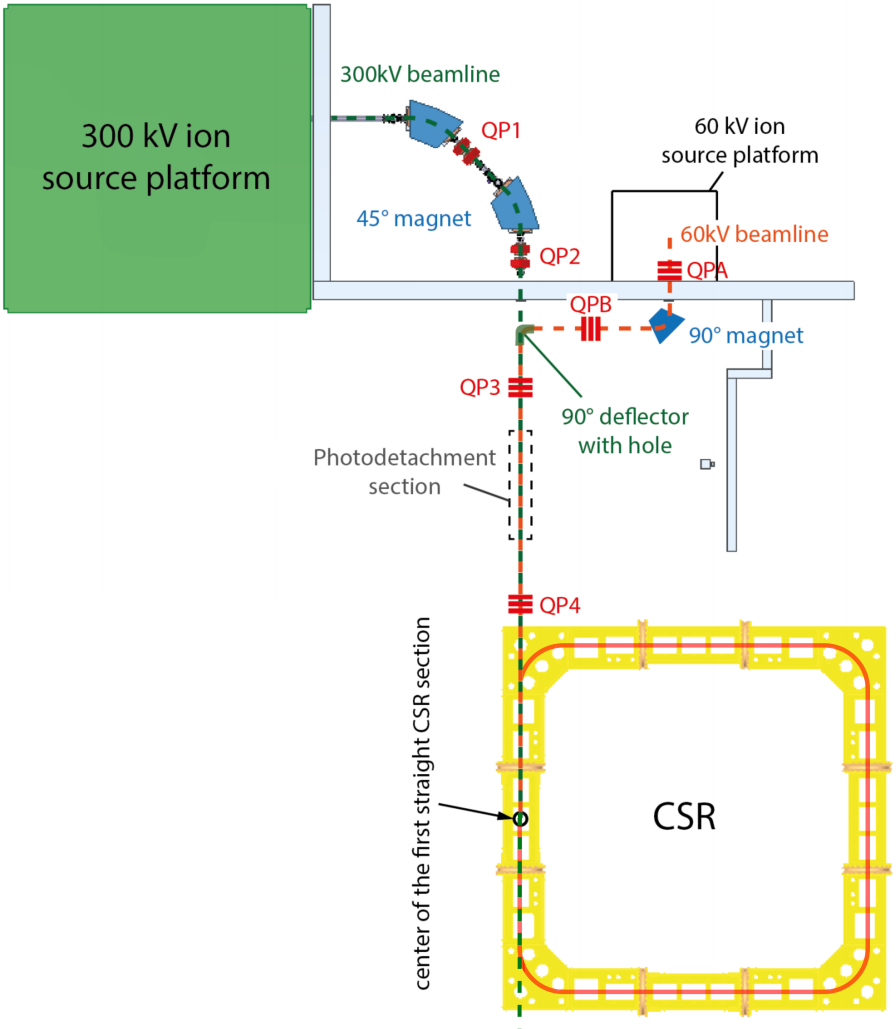

Figure 4.4: Schematic overview of the CSR transfer line, taken from [23]. Ion beams are generated and accelerated at 60 kV and/or 300 kV platforms, entering the storage ring guided by ion-optical elements. Dipole magnets and quadrupoles are represented by blue areas and red lines, respectively.

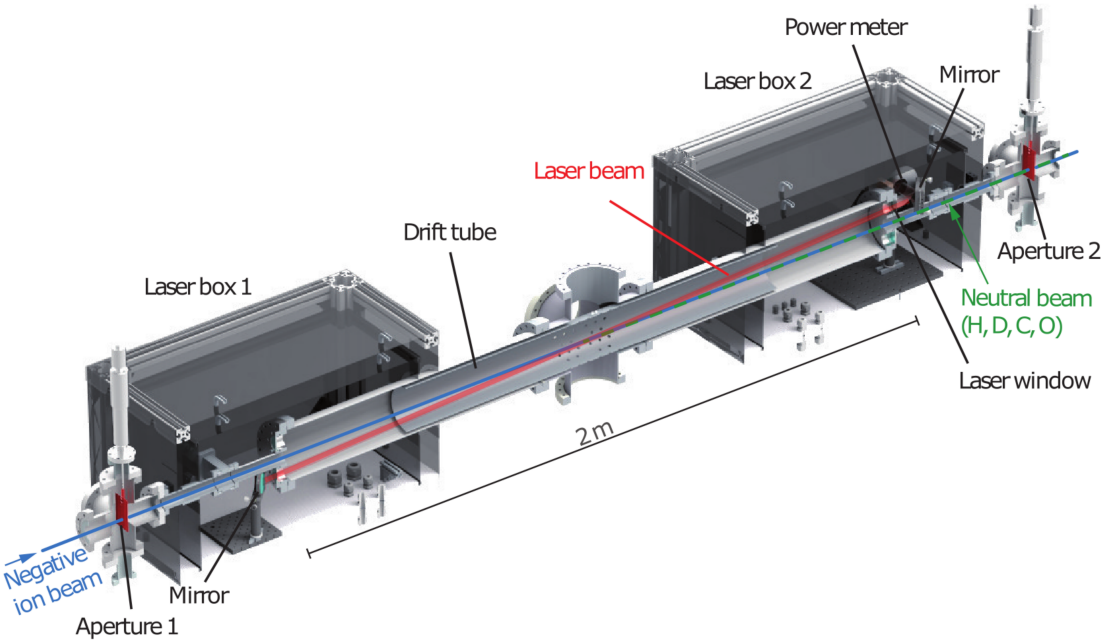

Figure 4.5: Schematic overview of the photodetachment chamber, taken from [23]. A laser (red) intersects the ion beam (blue) generating neutrals (green) due to photodetachment.

to hold a maximum voltage of 60 kV and 300 kV, respectively. To serve as an example, H_3^+ and C were used as ion-neutral reactants. In this case the H_3^+ would be generated at the 60 kV ion source, due to its lower mass. Before leaving the platform ions are accelerated to their final kinetic energy. A 90°-dipole magnet provides the mass separation of the ion beam. After crossing 4 focusing quadrupole doublets and a 90°-deflector the ion beam gets injected and stored in the CSR. Although the experiment aims for reactions between ions and neutrals, another ion beam (C^-) is generated at the 300 kV platform. This is because neutrals are unsuitable for accelerating and deflecting. Since we are interested in reactions at low relative velocity, the energies of the two platforms have to match such a way, that both ions leave the platforms with an equal velocity. In order to be as fast as H_3^+ with 51 keV, C^- requires the kinetic energy 202,7 keV. After leaving the 300 kV platform C^- gets mass separated at two 45°-dipole magnets.

At the photodetachment section a laser beam neutralizes a fraction of the C^- beam. The photodetachment process is able to create ground-state neutral atoms, which are required for relevant astrophysical reactions. In this process an anion absorbs a photon and subsequently eliminates an electron to form a neutral species. Inside

of the photodetachment chamber, depicted in Fig. 4.5, the laser beam is guided through laser windows into and out of the vacuum chamber. The ion beam, which propagates along the central axis of the PD chamber, is crossed by the laser beam. On entering and exiting the PD chamber the particle beam passes two circular apertures, which are separated by a distance of 2.9 m and have a diameter of 4.5 mm. These apertures constrain the shape of the neutral beam and collimate it. This is desirable for merged beams experiments, since it minimizes the relative collision angle and thus restricts and defines the center-of-mass collision energy.
The earth's magnetic field would force the ion beam inside the PD chamber onto a curved track. Hence, the neutral beam would leave the PD section slightly slanted. This is problematic since the neutral beam position cannot be corrected afterwards. To provide a straight neutral beam leaving the PD section, electromagnetic coils have been installed around the PD section, compensating the external field.
As mentioned previously, only a portion of the anions, transported through the PD chamber, are photodetached by the laser beam. This results in a particle beam consisting of anions and neutral atoms. In order to inject a pure neutral atomic beam into the CSR, the remaining anions have to be first removed. This has been done by a so-called beam-cleaner, a electrostatic deflector, only affecting the charged anions. At the first section of the CSR both neutral C and stored H_3^+ beams superpose at low relative energies. With this species the main interest lies on the reaction $H_3^+ + C \rightarrow CH^+ + H_2$ and its rate coefficient. As the merger product CH^+ has different charge to mass ratio than the stored ion H_3^+ it will leave the ring at the first CSR deflector. There, an energy-selecting electrostatic deflector isolates CH^+ before it hits the detector. From the detection count and the measured beam densities of the ion and neutral beam one finally can calculate the desired cross-section.

5 Simulation of Ion-Neutral Collisions

The fact that most rate constants have been measured at room temperature, not at the very cold temperatures of interstellar space, pushed the merged beams experiment at the CSR. In order to verify the collision conditions, namely the temperature, simulations were done. In the first step both ion and neutral beam profiles were calculated with G4beamline and Python, respectively.

5.1 Ion Beam Profile: G4beamline

G4beamline [24] was used to simulate the H_3^+ ion beam, stored in the CSR. It is a single-particle tracking and simulation program to model beamlines and experimental equipment. It handles a wide range of materials and fields, being particularly well suited for the study of muon and neutrino facilities. As it is based on the Geant4 toolkit [25], G4beamline includes most of what is known about the interactions of particles and matter. The basic structure of a simulation is to first define and place the beamline elements to be used, including their geometry, materials, and local fields. The following beamline elements were used in the CSR: 39°- and 6°-deflectors, quadrupole doublets and vertical steerer (Fig. 5.1). Electric and magnetic fields of the elements were calculated by Opera-3d [22]. For the simulation vertical steerer were only used in one half of the ring, being able to only correct the beam locally at the first straight section, were ion and neutral beam merge. Horizontal steering was achieved by tuning the 6°-deflectors. Eventually starting position and beam properties, as particle energy, particle species (H_3^+) and starting distribution (Gaussian), have to be set. Virtual detectors were placed along the collision region to sample the ion beam profile. As illustrated in Fig. 5.1, G4beamline provides the beam profile as a discrete distribution. For most simulations 481 equidistant placed detectors were used, covering 4,8 m where ion and neutral beam superpose.

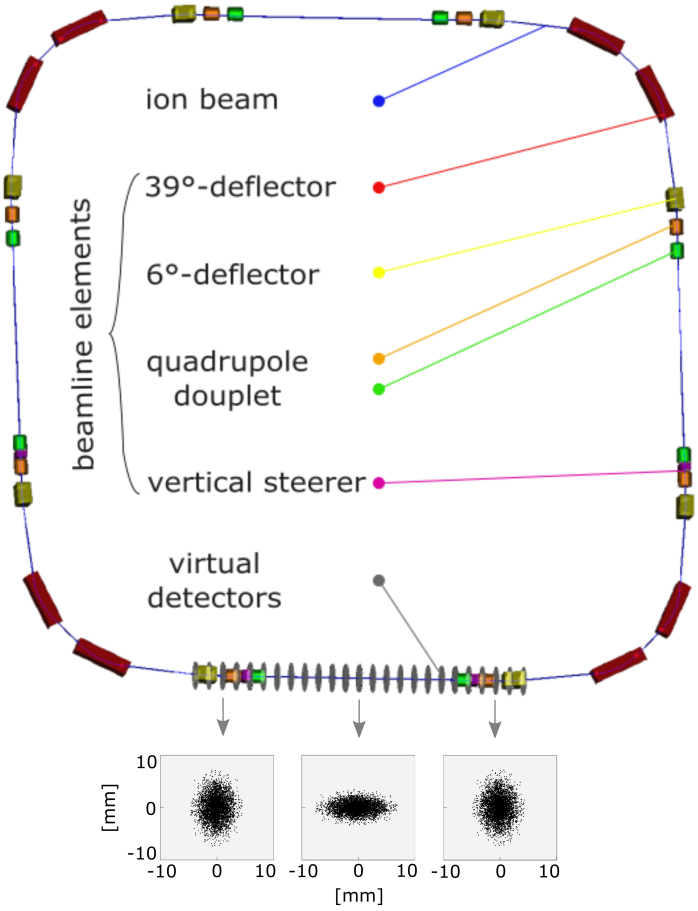

Figure 5.1: Visual output of G4beamline showing all beamline elements used for simulation. Additionally beam profiles, taken by virtual detectors, are presented.

5.2 Neutral Beam Profile: Python

Analogous to [26], a geometric approach was used to simulate the neutral beam. As illustrated in Fig. 4.5, the neutral beam is essentially limited by the geometry of the apertures at the photodetachment area. With the assumption that the incoming C^- beam homogeneously fills out aperture 1 a ray tracing model was used, shown in Fig. 5.2. We start by discretizing into pixels the plane in aperture 1 and the pseudoplane at the distance of interest behind aperture 2. The simulation then starts counting every pixel at aperture 1 seen from the pixels at the desired pseudoplane. The geometry of aperture 2 constrains the count number. The neutral beam profile at various distances to aperture 2 is presented in Fig. 5.3. The nature of the discretized approach implies that the total count number at the pseudoplane rises

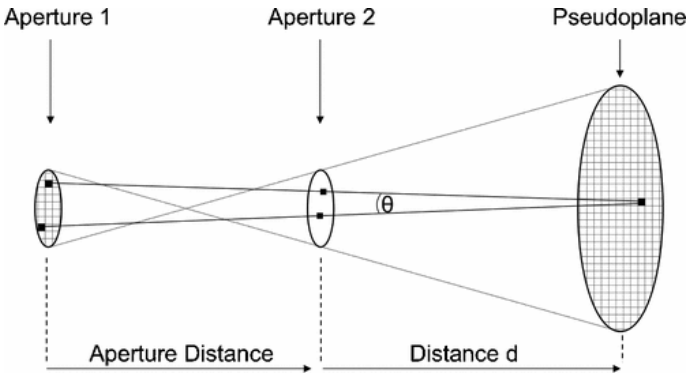

Figure 5.2: Geometric approach: The circular apertures at both end of the photodetachment are constraining the shape of the neutral beam [26].

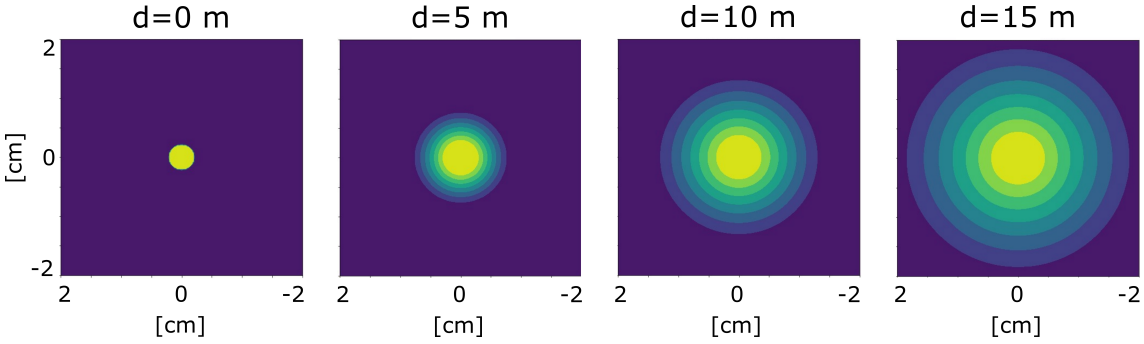

Figure 5.3: Beam profile of neutral beam at several distances d to the photodetachment section. Linearly scaled and in arbitrary units. In order to grasp the experiment properly, the profiles still need to be normalized.

with increasing distance to the PD section. However, with no particle losses in the experiment the particle count should stay constant along the beamline. Hence, the beamprofiles have to be normalized afterwards.

5.3 Calculating the Collision Energy

In the non-relativistic limit, the relative energy in the center-of-mass frame E_r is given by [27]

$$E_r = \mu \left(\frac{E_{H_3^+}}{m_{H_3^+}} + \frac{E_C}{m_C} - 2\sqrt{\frac{E_{H_3^+} E_C}{m_{H_3^+} m_C}} \cos\theta \right), \tag{5.1}$$

where $m_{H_3^+}$ and m_C are the masses of H_3^+ and C, respectively, μ is the reduced mass of the colliding system, and θ is the angle of intersection. According to the formula even collision energies of $E = 0\,eV$ can be reached. To accomplish this, first both

beams have to be velocity-matched perfectly, leading to equal energy to mass ratios for both species. Moreover, the root can be extracted, yielding the same energy to mass ratio. Second, the intersection angle θ has to be equal to zero by which means $\cos\theta = 1$ and thus the whole bracket equals to zero. In the case of a realistic merged beams experiment collision energies on the order of a few meV are feasible. The energies are mainly limited by the spread in collision angles between the two beams [27].

Fig. 5.4 gives an overview about simulation steps performed in order to gain the collision temperature. To get an energy distribution representing all possible collisions at the merged beams experiment, all their energies have to be summarized, weighted by their probability. This has been done by picking one particle from the g4bl detector and calculating the collision energies between this ion and every neutral (given by the Python code simulating the neutral beam) that reached the ion position from its pixel at aperture 1, taking into account the relative collision energy and angle. Afterwards this step was repeated until all particles at every detector from the g4bl simulation have been covered. To get a temperature estimate from the energy distribution a Maxwell–Boltzmann distribution was fitted.

The energy dependency of the distribution p, required for the fit, was derived from [28]:

$$p(v)dv = \left(\frac{m}{2\pi kT}\right)^{3/2} 4\pi v^2 \exp\left(\frac{-mv^2}{2kT}\right) dv, \tag{5.2}$$

where m is the particle mass and kT the product of the Boltzmann constant $k = 8.617 \cdot 10^{-5} eV \cdot K^{-1}$ and the thermodynamic temperature. Deduced from the kinetic energy $\mathrm{E_{kin}} = mv^2/2$ the substitutions $v = \sqrt{2E/m}$ and $dv = dE/\sqrt{2mE}$ yield the desired dependency

$$p(E) = 2\sqrt{\frac{E}{\pi}} \left(\frac{1}{kT}\right)^{3/2} \exp\left(\frac{-E}{kT}\right), \tag{5.3}$$

where E and T denote the collision energy and temperature, respectively. To be able to fit the distribution to the histogram it was multiplied by a scaling constant c, because arbitrary units were used in the histogram. Since histograms with logarithmic energy scales will be used, the bin width varies proportional to the interaction energy. Thus, bins at higher energy gather collisions in a higher energy range. To compensate for that the fitted Maxwell–Boltzmann distribution has to be additionally multiplied by the factor E_{kin}.

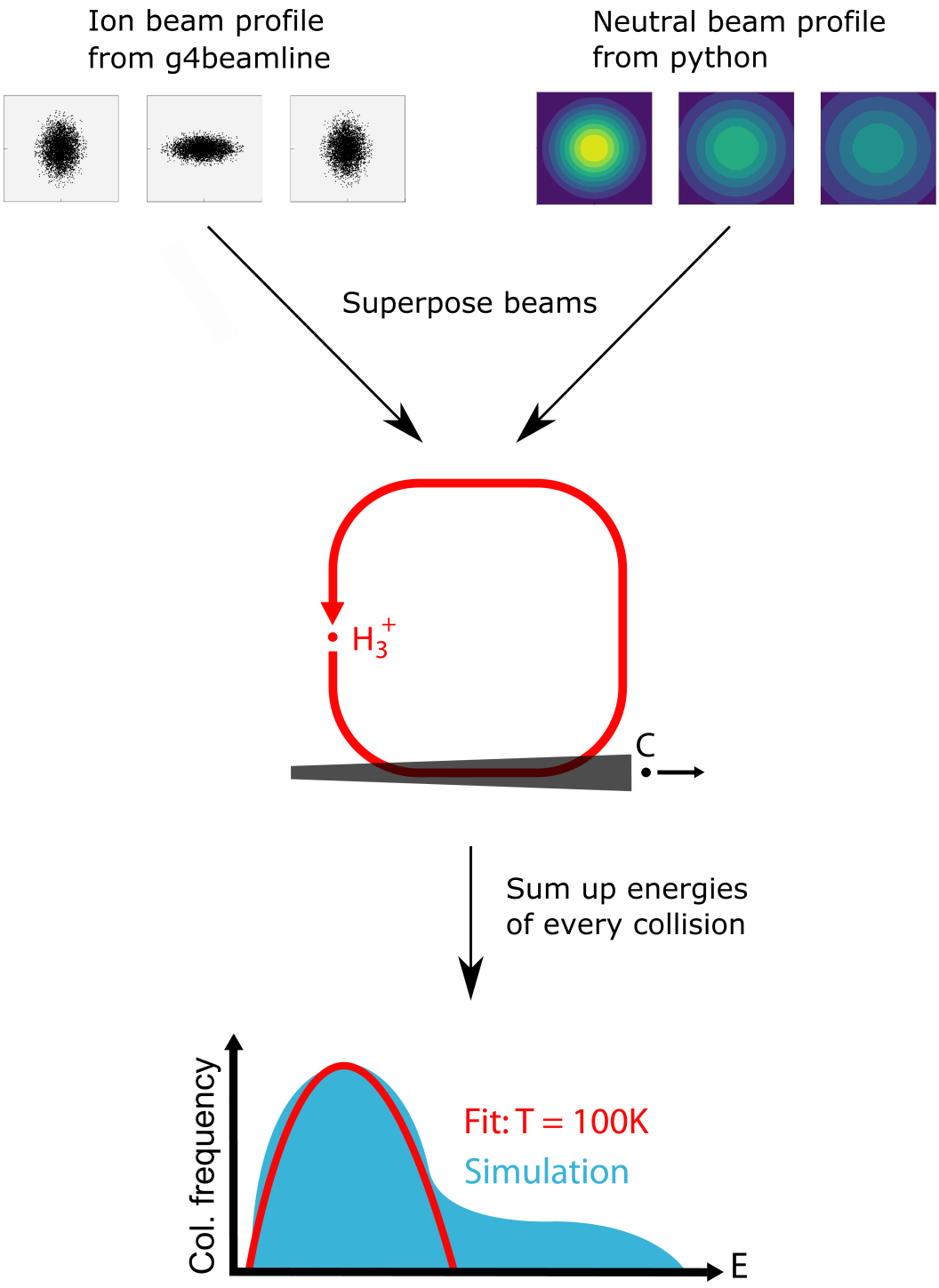

Figure 5.4: Overview of the way, how collision temperatures are gained from the simulation. First both ion and neutral beam profiles were calculated with G4beamline and Python respectively. Subsequently both beams were superposed and the energy of every collision was summed up. To get a temperature estimate a Maxwell–Boltzmann distribution fit for the low energy part of the distribution was used.

5.4 Examples

Using the example of superposed H_3^+ and C we want to investigate the collisional energy distribution. A best case scenario is presented as a limit for the lowest attainable energies. Additionally, it will serve as a basis where other effect will be examined by only varying one property of the beam or the environment. Particularly, a velocity spread of the beams, different ion beam emittance's and the effect of the earth's magnetic field was considered. Finally, a realistic combination of all the effects is presented.

Best Case Scenario

In order to understand the features at the energy distribution we first want to look at the best case scenario. More specifically, both beams share exactly the same velocity, the impact of the earth's magnetic field on stored H_3^+ ions was neglected completely and the starting emittance of the stored beam is equal to zero, resulting in a point-like cross section of the beam. Fig. 5.5 displays a collision energies for our best case on the top panel and the corresponding beam shapes at the intersection region in the bottom. Horizontal beam broadening is a consequence of computational accuracy. Collisions at the center drift section between the quadrupole doublets have low energies, forming the peak 1 meV. The quadrupole doublets focus the charged beam leading to increased intersection angles, thus also higher collision energies. The bump at 10 meV has its origin in collisions at the quadrupole doublets. The discrete peaks at high energies originate from the 6°-deflectors. With raising ion beam angle the energy increases. Since virtual detectors are placed every 10 mm, falsely discrete energies are computed. Fitting the Maxwell–Boltzmann probability distribution $p(E)$ results in a 9 K mean collision temperature, as a lowest reachable limit.

As no sharp resonances and maxima are expected for ion-neutral reactions, usually peaks at high energies will not dominate. In every simulated scenario they make up $\sim$11% of all reactions. Since they can be included in the analysis of energy dependent experiments, these experiments are mainly limited by the low energy part of the distribution. As a consequence it is reasonable to fit the Maxwell–Boltzmann distribution only to low energy part.

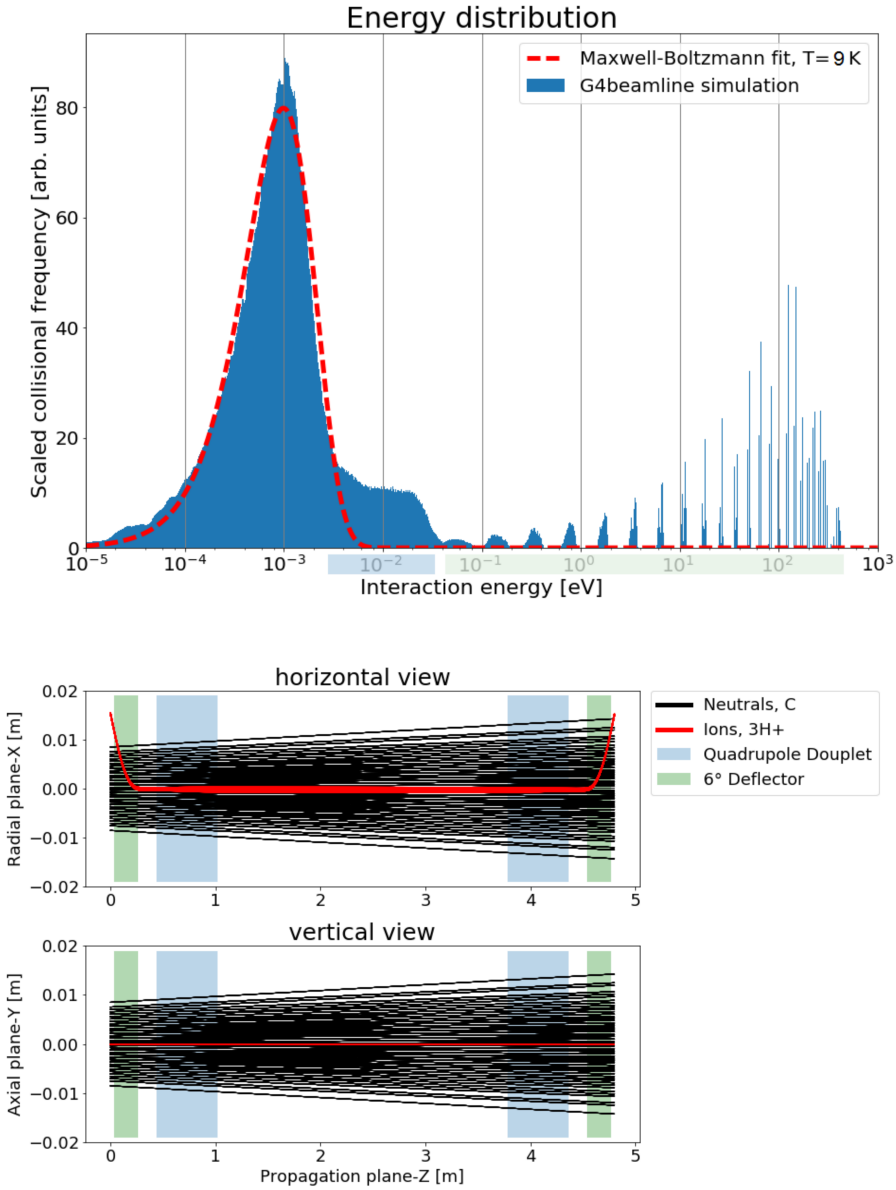

Figure 5.5: Histogram of collision energies (top) and interaction region (bottom) for the best case scenario. Particularly, no velocity distribution on both beams, a point-like ion beam cross section and no effects from the earth's magnetic field.

Velocity Spread of the Beams

Equation 5.1 suggests a dependence of a velocity mismatch between the beam on the collision energy. In reality, both the ion and the neutral beam possess a velocity spread of about 10 eV. Fig. 5.6 shows a modified best case scenario where the neutral beam energy has a normal distribution with a standard deviation of 30 eV. While this permits collision energies below $\sim$0.2 meV, the overestimated velocity spread shows only a minor effect on the resulting collision temperature. As the neutral beam trajectories are gained from a geometric approach the energy difference does not change the particle paths. However a energy spread of $\sigma = 30$ eV on the ion beam neither alters its trajectory noticeably and the effect on the energy distribution is similar to the displayed one. It should be noted that there is a specific reason why the histogram in Fig. 5.6 uses larger bins and appears pixelated. It helps to grasp the relations of the high energy tail, which was hampered by peaks, originating from individual virtual detectors.

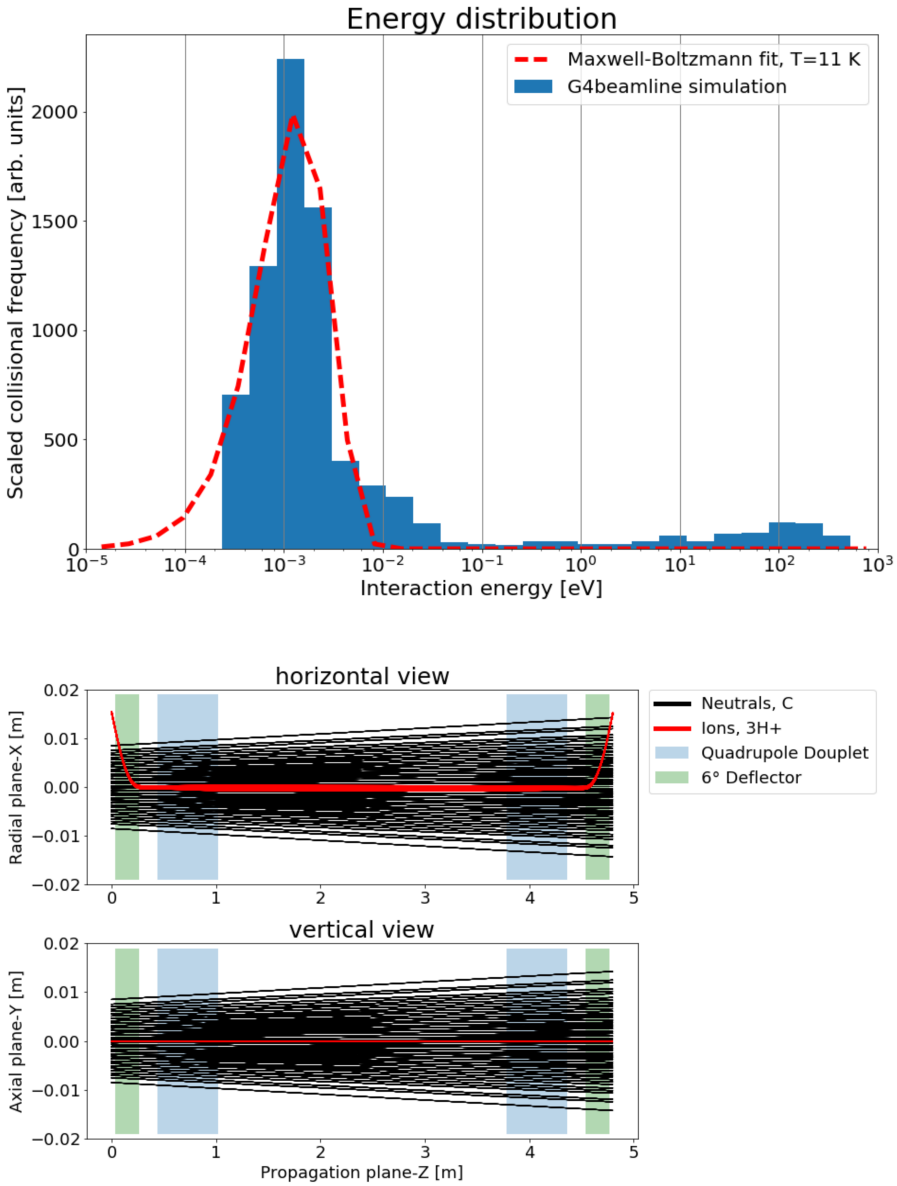

Figure 5.6: Varying the best case scenario (see Fig. 5.5) by giving the neutral beam a gaussian velocity spread of $\sigma = 30$ eV.

Beam Shape

While the cross section in our best case scenario is point-like this is far from realistic. Already the injected ion beam possesses a certain emittance. While Liouville´s theorem states that the total phase area is conserved, this is true only when solely using linear ion-optical elements. Non-linear elements, as the focusing quadrupoles, lead to a distortion of the phase space distribution, called filamentation, which can lead to an increase of the effective emittance.
The results in Fig. 5.7 were obtained by changing the point-like ion beam from the best case scenario to a natural shape. Since the beam shape inside the CSR is mostly limited by the injection line acceptance, it fills the inner vacuum chamber of the CSR only partially. Thus, in Fig. 5.7 the standard deviation σ_x and σ_v for initial position and velocity spread correspond to only 6 % of the rings acceptance. With a horizontal ion beam width of approximately 2 cm at the section center, it has a similar spatial spread as the neutral beam. Being that broad the focusing effect of the quadrupoles can be observed nicely. With an enhanced spatial spread like this, collision angles raise and thereby collision energies do too. This can be observed at the main peak and the quadrupole bump, both shifting to higher energies. In total the collisional temperature increases to 209 K.
While choosing 6% of the CSR acceptance as starting condition might capture the properties of an ordinary stored ion beam it may still be interesting to investigate different beam shapes. Particularly, as the CSR houses an electron cooler capable of phase-space cooling the stored ion beam. Assuming that the cooling effect reduces the beam size so that starting condition decreases to 2% of the CSR acceptance, simulations predict a horizontal beam width of $\sim$5 mm at the section center. Furthermore the Maxwell-Boltzmann fit predicts collision temperatures of 31 K, which lays perfectly in the desired temperature regime of 10-100 K.

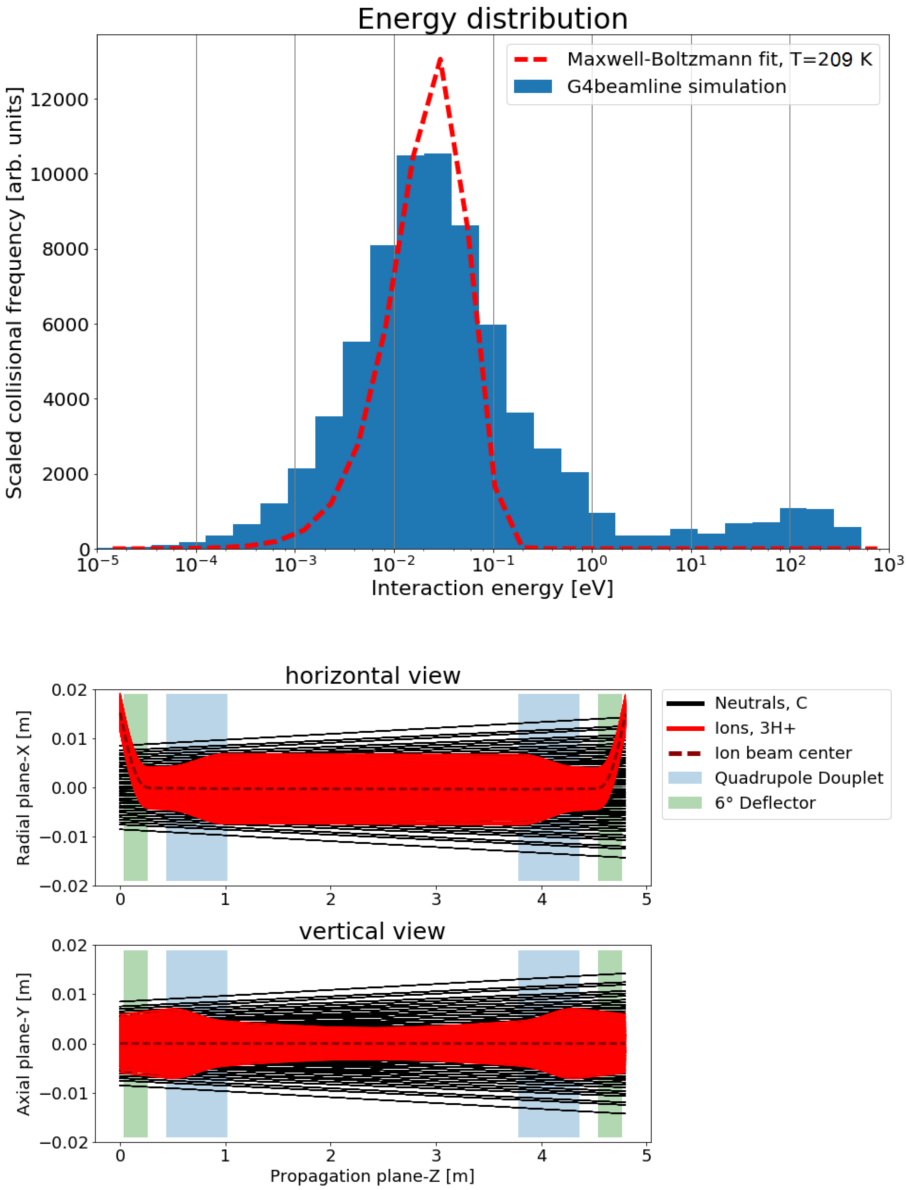

Figure 5.7: Varying the best case scenario (see Fig. 5.5) by increasing the beam emittance from point-like to 6 % of the beams acceptance.

Earth's Magnetic Field

At last we want to have a look at the effect of the earth's magnetic field. Since magnetic fields force stored ions on curved trajectories, storing becomes more difficult for ions with either a lower mass to charge ratio or low energies. As H_3^+ is a relatively light ion, significant effects of the earth's magnetic field will be expected. For the first assessment a globally homogeneous field $|\mathbf{B}_{\text{earth}}| = 51.5$ µT was assumed. This initial coarse value resulted from a mean of measurement series around the ring with a Hall effect sensor. Strikingly the ion beam has shifted and bend (Fig. 5.8). The collision energy does not only raise but also shows a different distribution. Two small peaks appear on the right side of the main peak. The two peaks could be identified with the two Quadrupole regions, where collision energies occur due to the slanted ion beam. The difference in the vertical component is the crucial part for the appearance of two discrete peaks. While being higher on the left quadrupole, the peak can be observed at higher energies. Due to the two prominent quadrupole peaks it becomes unsuitable to find the collision temperature with a Maxwell-Boltzmann fit. In this case only the main peak originating from collisions at the center region between the quadrupole doublets is captured by the fit.
Since ion beam displacement can be corrected, this consequence of the earth's magnetic field can be compensated. Correction can been done with help of vertical steerers, installed between 6°-deflectors and quadrupole doublets, and moreover by tuning the applied voltage at the 6°-deflectors. It should be noted, that corrections cover displacements in position and angle. Fig. 5.9 shows the result of a locally corrected ion beam. The ion beam remains curved, but is centered now. The correction yields the collision temperature T = 586 K.

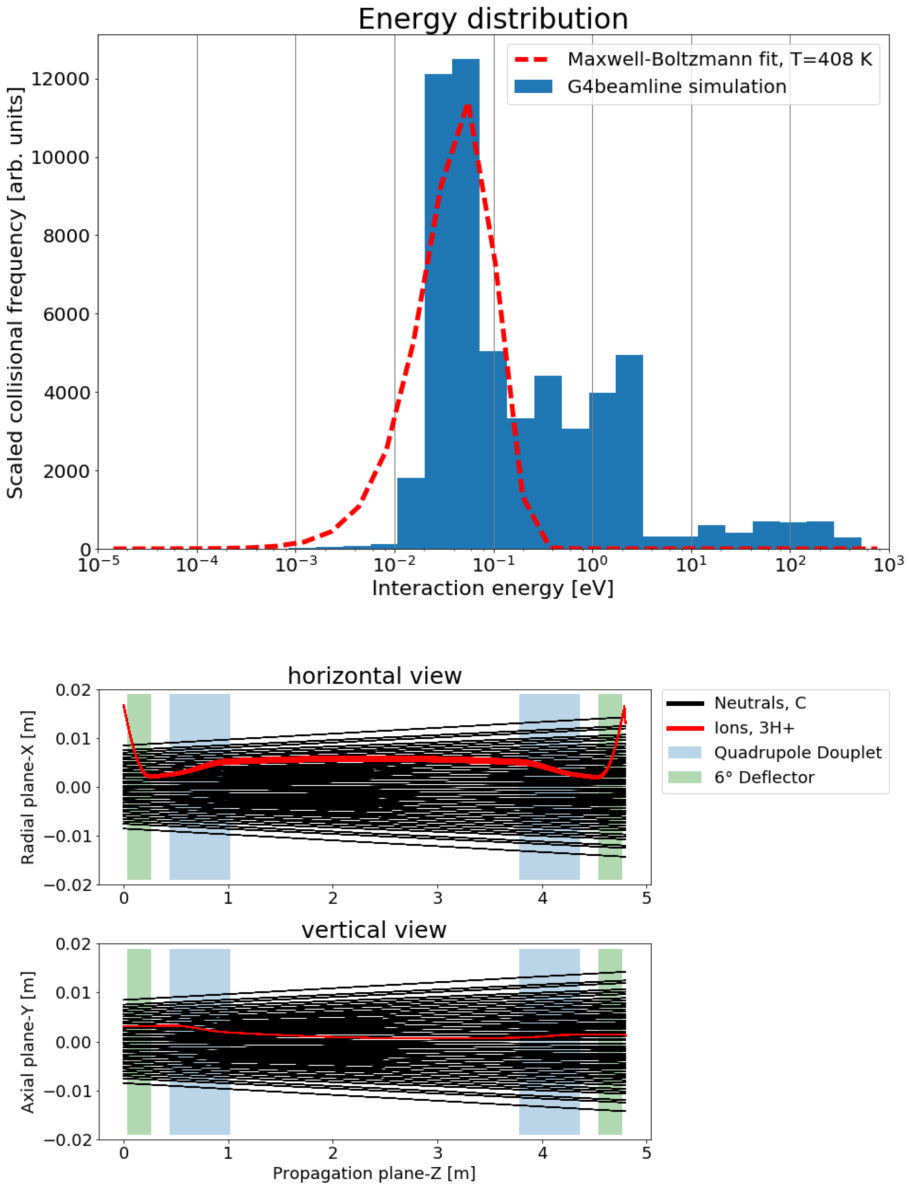

Figure 5.8: Varying the best case scenario (see Fig. 5.5) by enabling a homogeneous magnetic field $|\mathbf{B}_{\text{earth}}| = 51.5\ \mu\text{T}$ to interact with the ion beam. The ion beam gets shifted especially horizontally.

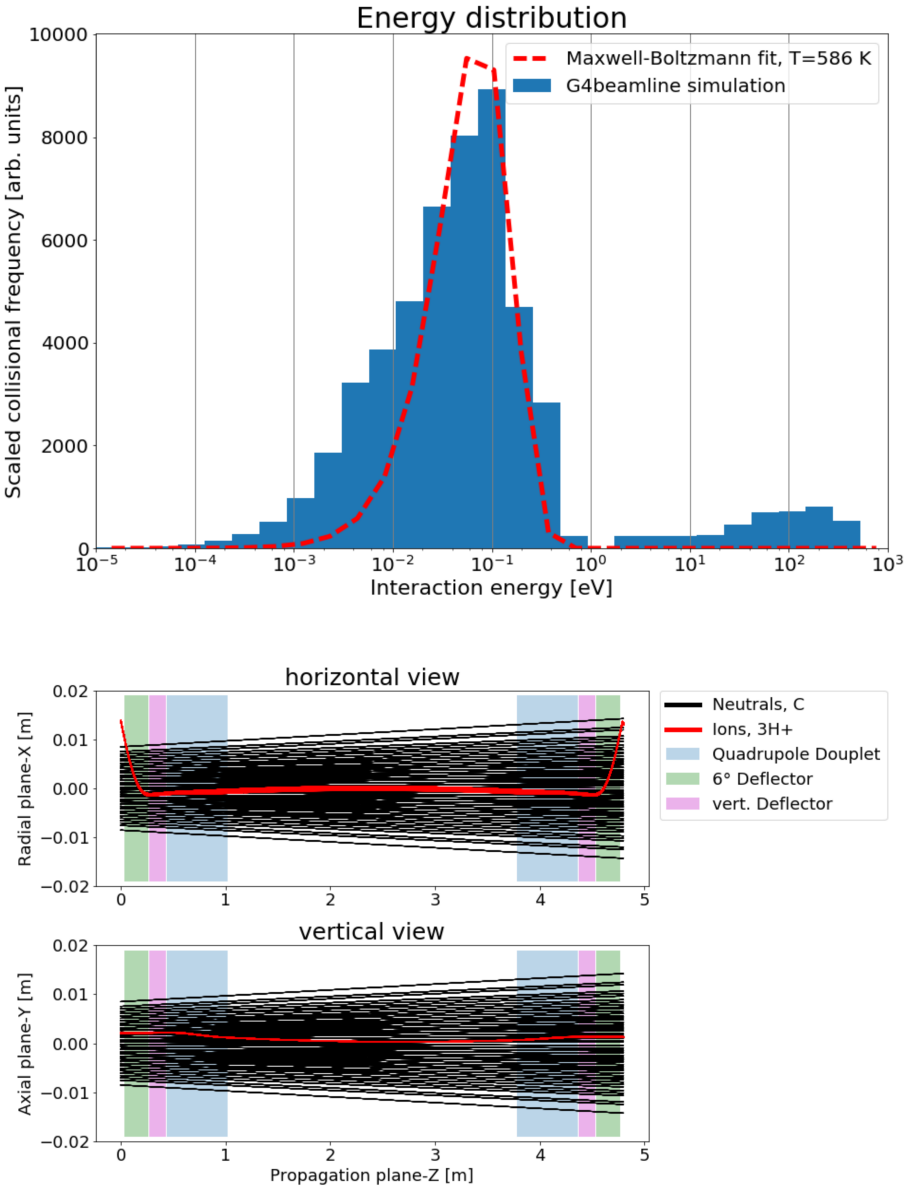

Figure 5.9: Varying the best case scenario (see Fig. 5.5) by enabling a homogeneous magnetic field $|\mathbf{B}_{\text{earth}}| = 51.5$ µT to interact with the ion beam. Vertical Steerer (purple) and 6°-deflectors (green) were used to direct the beam to the center.

Collisions under realistic conditions

In the previous subchapters various effects were examined individually. In reality they show up together to some degree. Table 5.10 gathers the results for different compositions. Considering the earth's magnetic field $|\mathbf{B}_{\text{earth}}| = 51.5$ µT, a spread ion beam filling 6 % of the rings acceptance and a velocity deviation $\sigma_E = 10$ eV on both beams, a high collision temperature T = 614 K will be reached. To tackle this undesirable high temperature we want to lower the impact of the earth's magnetic field inside the CSR. It is foreseen to install electromagnetic coils around the entire ring, the same way as it has been done in the photodetachment area. They would produce a magnetic field with the same strength as the earth's magnetic field but oriented in the opposite direction, reducing the magnetic field inside the CSR ideally to zero. Taking the assumption that the earth's magnetic field can be reduced at the whole ring to 10% of its former strength the temperature T = 209 K would drop significantly. Even reduction rates of 25% and 50% show a huge improvement temperature wise.

Since it is more efficient in time and resources to install electromagnetic coils only at one straight section, this case also was calculated. Reducing the earth's magnetic field to 10% only at the straight line of the CSR where the ion-neutral collisions happen, a huge temperature drop to T = 280 K has been recorded. An unrealistic point-like beam shows the impact of local field compensation at the collision area, where temperatures of T = 22 K can be expected.

The achievable temperatures under realistic conditions presumably lie somewhere

Starting ε of ion beam	0% B_{earth}	10% B_{earth}	25% B_{earth}	50% B_{earth}	100% B_{earth}		100% B_{earth} + reduction of B_{earth} at col. section to:	
							50%	10%
point-like	9 K	11 K	37 K	145 K	586 K	408K	121 K	22 K
2%	31 K	136 K						
4%	98 K	196 K						
6% of acceptance	209 K	209 K	232 K	310 K	614 K		344 K	280 K

Figure 5.10: Collisional temperatures for various settings. The orange one indicates, that a velocity distribution of $\sigma_E = 10$ eV was considered on both beams. The green background indicates, that no steerer nor 6°-deflectors have been used to ensure a centered beam. Without correction the Maxwell-Boltzmann fit suggest a collision temperature to low, as discussed in chapter 5.4.

between these values As one section in the CSR is dedicated to cool the stored ion beam probably beam shapes corresponding to 2% of the ring acceptance can be stored. In the case of a global magnetic field reduction to 10% of its former strength this would lead to collision temperatures T = 136 K, being the most realistic collision temperature assessment. Still the beam shape exhibits unresolved problems, because it has not been measured precisely although the collision temperature shows a strong dependence on it. It should be noted that the case studied here (collisions of H_3^+ on C) shows a particularly strong influence of the earth's magnetic field, since the maximum energy is limited by the small ion source platform and we are dealing with a relatively light ion.

6 Precise Earth's magnetic field measurement

As discussed in the previous chapter the earth's magnetic field has a strong influence on the stored ion beam. This alone should be enough incentive to determine the magnetic field accurately. But also the magnetic field compensation inside the CSR requires detailed knowledge.
In order to acquire a detailed and accurate magnetic field map around the CSR the fluxgate magnetometer AS-U3D GEO-X [29] was used. There, for every coordinate axis a magnetically susceptible core is wrapped by two coils. A periodic electric current is passed through the first coil, driving the core periodically in magnetic saturation. In the absence of a background field the induced electric current in the second coil matches with the input current. Otherwise a signal can be measured in the second coil proportional to the vectorial component of the magnetic background field. In our case a magnetic fluxes from 0.01 µT up to 200 µT could be measured in every Cartesian spatial direction simultaneously. A linearity error of $<$0,8% $\pm$0.2 µT has to be considered. Despite the accuracy of the probe it may possess an offset, which is stable in a span of a day, but may change over longer time scales or when it is exposed to strong magnetic field strengths ($\geq$200 µT).

Figure 6.1: AS-U3D GEO-X [29], the magnetometer used to determine the magnetic field precisely.

6.1 CSR

As motivated in chapter 5.4 it is beneficial to have the stored ion beam exposed to a minimum external magnetic field. To compensate the external field it has to be known at first, preferably at the position of the stored ion beam. The problem is, that the beamline itself is hardly accessible, due to the inner and outer vacuum chamber and the 40 K and the 80 K radiation shield enveloping it. Therefore the field was measured at serveral points outside of the CSR chamber. As care was taken to only use non-magnetic materials for the CSR construction it should be possible to reasonable assess the field inside the CSR.
Fig. 6.2 illustrates the locations of measurement and the measured magnetic field values. For all measurements the big crane at the CSR hall was positioned above the e-cool section of the Test Storage Ring TSR, since it influences the magnetic field. Normally 4 measurements were taken per cut, one at every corner. Corners bear the advantage to be cut-in, aligning the cubic magnetometer automatically, thus ensuring a measurement of the same field components at every location. Measurement cuts were taken every 40 cm.

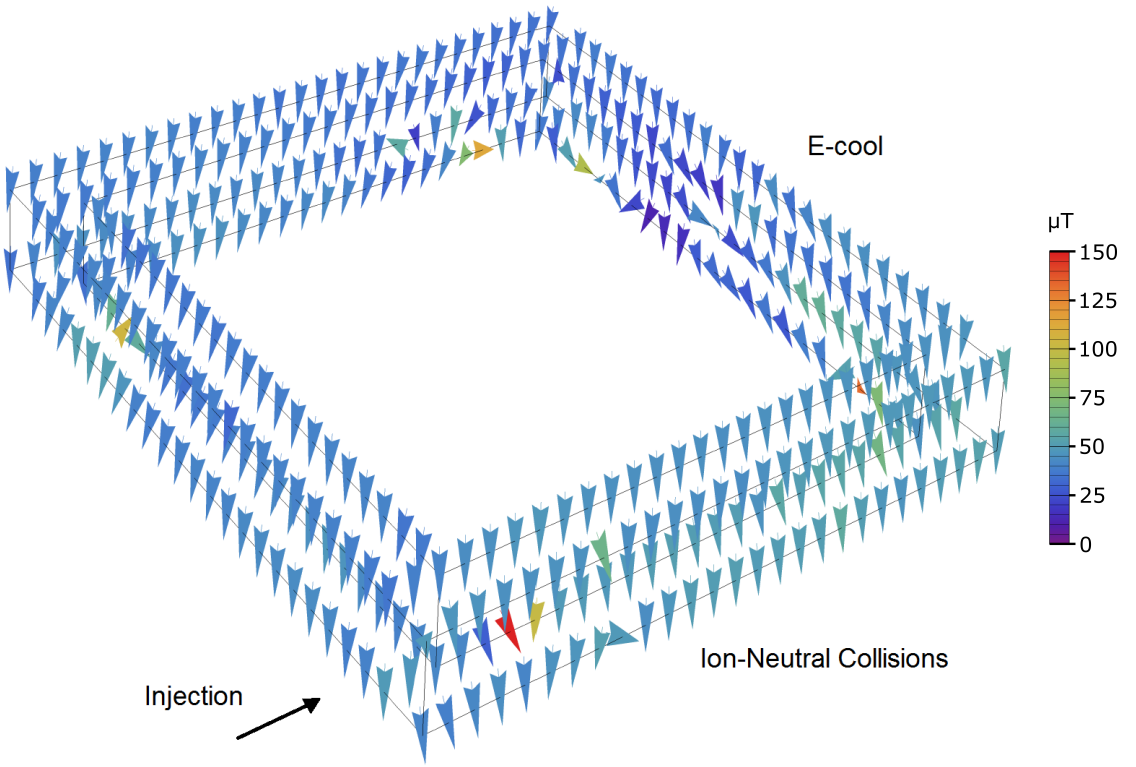

Figure 6.2: Illustration of all measured points and magnetic field values.

It was considered to take measurement points not at the edges, but at each side: left and right of the ring as well as above and beneath. They would have a favourable position as they sit closer to the ion beam than the measurement points at the edges. The reason why the edge points were chosen over the side points are due to the following difficulties coming with the side points. First, without the cut-in at the edges, measurements at the side of the CSR can not ensure a proper magnetometer alignment. Second, often the side positions are blocked by experiments, as it is the case with ecool or the cryocooler. Moreover taking measurements on the bottom side of the CSR often is hampered by surface irregularities and the existence of pillars and wires.
Another possibility is to straight take 8 measurement points per cut, 4 at the edges and 4 at sides. However, comparing the results from 4 and 8 data points show only marginal differences for field at ion beams position, making the effort to take 8 over 4 edge data points unappealing. It should be noted that unlike suggested in Fig. 6.2 measurement points could not be taken equidistantly. Mainly perturbed by the geometry of the CSR corners and central part of the straight regions, measurement points deviate up to 15 cm from the desired location.

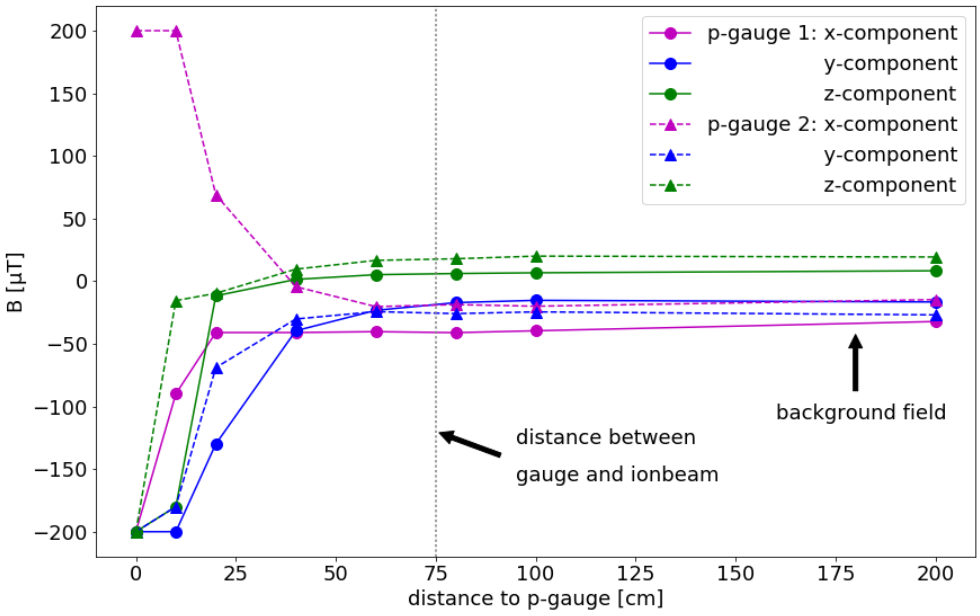

Figure 6.3: Range of influence of pressure gauges, installed underneath the CSR, on the magnetic field .

Fig. 6.2 implies a relatively homogeneous magnetic field around the CSR. Noticeable are the low values at the e-cool region incorporating iron. Thus, making an estimate for the central field insufficient. Furthermore, extremely high magnetic fields close to the corners are conspicuous. That is because pressure gauges are installed next to each corner underneath the CSR, which contain magnets themselves. Fig. 6.3 displays the range of influence on the magnetic field of these pressure gauges. Several locations placed in a straight line from 2 different gauges were measured. Although the effect close to the gauges is huge, it declines rapidly with increasing distance. The ion beam has a minimal distance of 75 mm to the gauges. At that

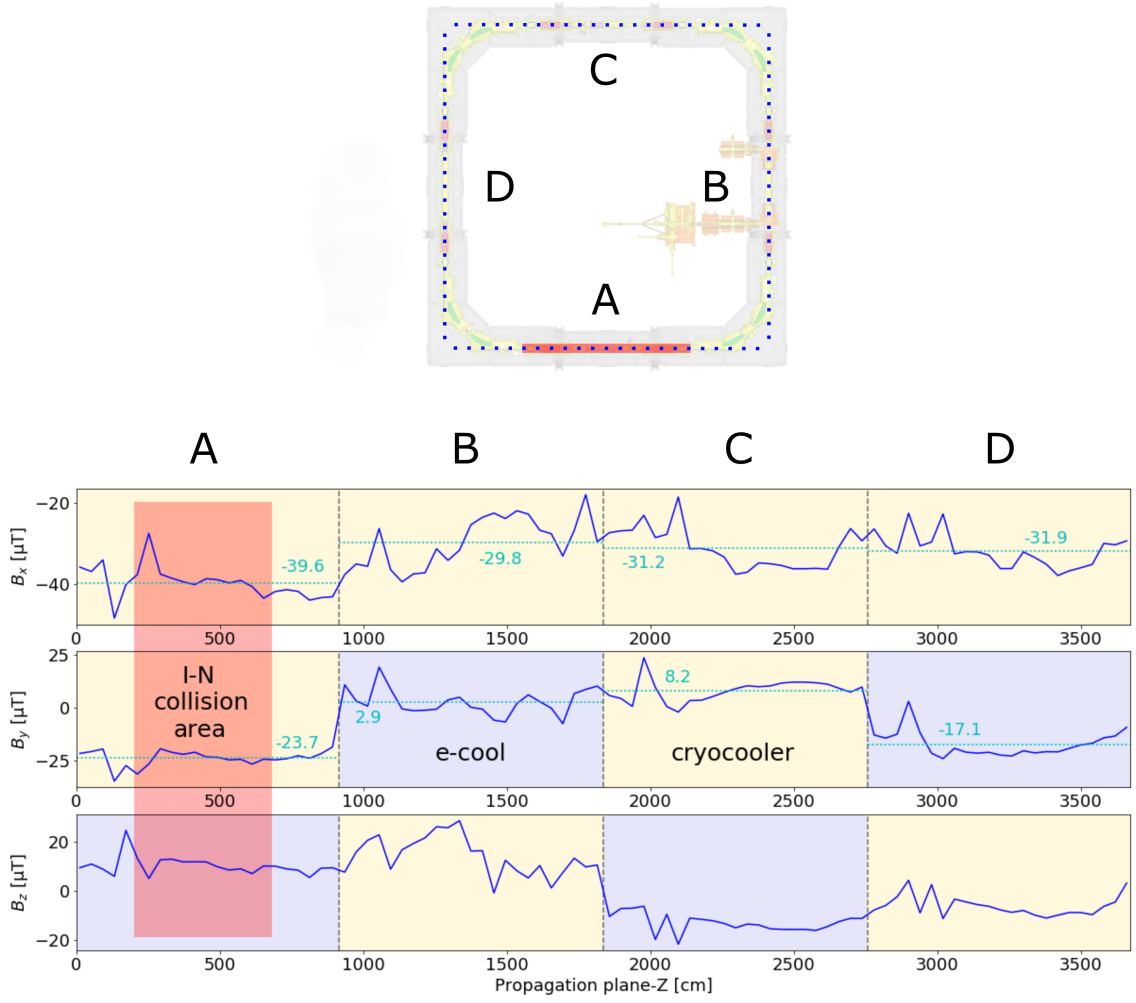

Figure 6.4: Magnetic field strengths inside the CSR were calculated from the values measured at the CSR casing. Each blue dot indicates their location. The red box marks the area where ion neutral collisions actually may happen.

distance almost no effect on the background field can be recorded.
Fig. 6.4 features the magnetic field inside the CSR. A weighted mean was taken from all measured points from one cut (see 6.2). It was weighted with $1/r^3$, where r is the distance from the data points to the beam. The blue dots in the upper panel indicate the positions where the mean was calculated from the measurements. Since the positions are aligned in a line, they deviate from the ion beam position in the CSR corners. In the bottom panel the mean values were plotted for each component. A local coordinate system was used in every straight section. Moving counter-clockwise with the ion beam the x-axis always points up, the y-axis always to the left and the z-axis always opposed to the direction of the ion beam. Only magnetic fields with a component orthogonal to the ion beam are able to affect it due to the Lorentz force. Hence, compensation coils around the CSR only would need to compensate these components and can neglect the z-component in our case. Thus, a mean has been calculated for the x- and y-component for every straight section indicated by dotted cyan line. Since local coordinates have been used, the y- and z-axis show in different directions at every straight CSR section. To identify matching global coordinate sections y- and z-components are coloured alternatingly. The red box marks the area where ion neutral collisions actually may happen.
The outlier at the start of each straight section originate from the pressure gauge installed beneath the CSR casing. Even if Fig. 6.3 implies no effect magnetic field inside the CSR, the mean was calculated from all 4 edge data points. This could lead to overestimate of the influence of the pressure gauges. More realistic results may be obtained by ignoring the data points influenced by the pressure gauge. However, the pressure gauge seems to change the magnetic field both to the negative and the positive, lowering the final influence on the straight section mean.
Furthermore inhomogeneity can be observed on CSR scales. The x-component seems to be stronger by 9 µT in the ion-neutral collision section than in the others. The y- and z-components show a inhomogeneous trend too, since otherwise the magnetic field strength in section A and B should be equal to the negative strength in section C and D, respectively. In the end, a distance weighted mean at the ion beam positions yields a magnetic field strength of 39 µT $\pm$ 8 µT.

6.2 Peripheral Effects

Construction Hall Crane

The construction hall, housing the CSR, contains a crane, which can be seen in Fig. 6.5. It is assumed that the crane has a significant influence on the magnetic field at the CSR since it is almost fully constituted of iron. Hence, in the previous measurements, attention was paid to place the crane always at the same position, the e-cool section of the TSR. In order to gauge the impact of crane position on the magnetic field at the CSR several positions were examined. This was done with both a stationary and a moving crane.

Fig. 6.6 depicts measurements for a stationary crane at different positions, where 0 m marks the position directly over the ion-neutral CSR section. The magnetic field variations were measured at the two straight sections of the CSR parallel to the crane. At the diagnostic section measurements at 3 different cuts were taken, 4 measurements at every edge per cut. The first cut was located at the center and the others at a distance of 1.6 m. At the ion-neutral collision section measurements at 5 different cuts were taken. Again, the first cut was located at the center but the others in a distance of 1.6 m and 3.2 m. To take the crane's influence on the whole section into account Fig. 6.6 displays the mean of all measurements at a specific crane positions for both sections. The influence on the ion-neutral section (blue straight line) is rather symmetrical and lowers with the distance to it. The beam

Figure 6.5: Crane (yellow) placed next to the CSR.

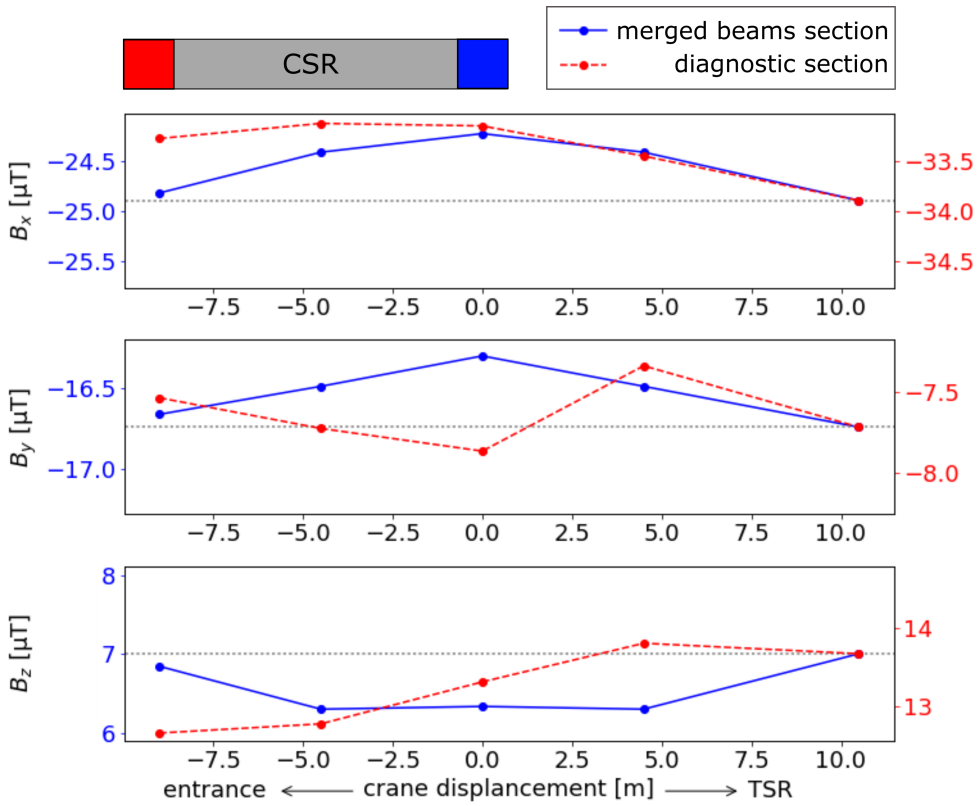

Figure 6.6: **B** field measurement taken for different crane positions at two straight CSR sections. The relative position of the CSR and both of its examined sections are illustrated at the top. Each blue dot represents the mean of 20 measurements along the ion-neutral collision section. At the diagnostic section (red) 12 measurements were taken per crane position. Field strengths can be read at the appropriate axis, marked in the same color. The grey dotted vertical line was set to the value at the initial position over the e-cool section of the TSR.

diagnostic section is located at ∼-10 m. There, the same trend can be observed (red dashed line), the crane's influence increases with decreasing distance. Only the y-component reveals a strange behaviour. In general the crane position changes the magnetic field strength up to 0.7 µT.

Fig. 6.7 displays measurements for a moving crane. The magnetic field was measured at the center of the collision section on top of the CSR. The crane was moved from a position close to the entrance of the construction hall (-9 m) to a position over the TSR (9 m) back and forth. The position exactly above the collision section corresponds again to the 0 m mark. The arrows indicate the direction the crane is moving to. Each dot represents one measurement, which was taken every 2 seconds.

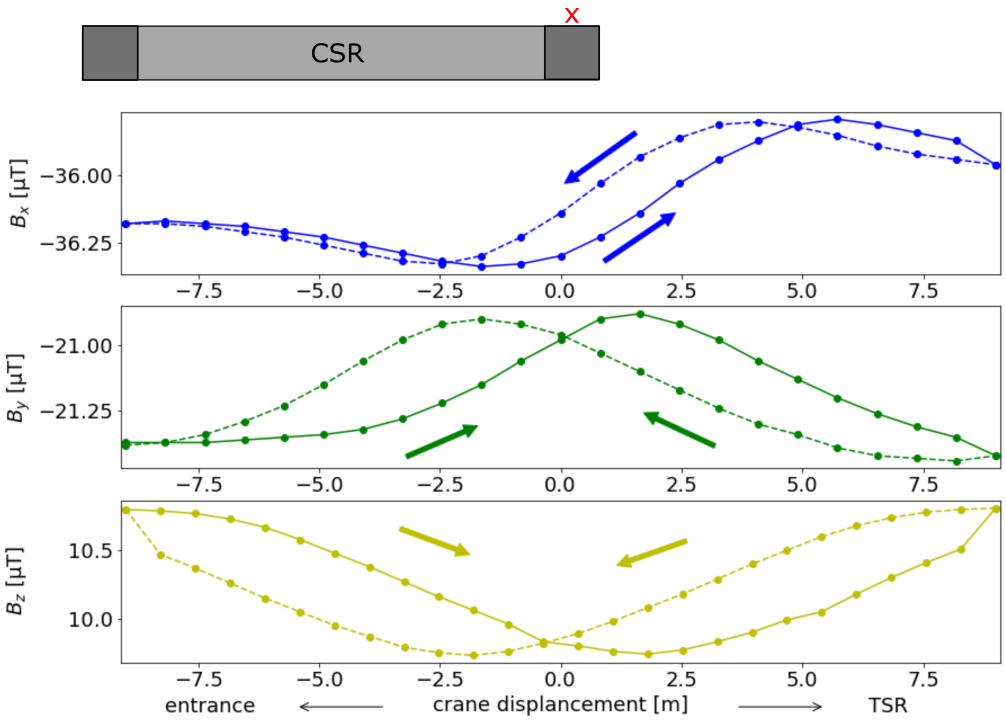

Figure 6.7: Magnetic field **B** measured under the interference of a moving crane. The measurement location, at the center on top of the CSR collision section, is marked with a red "x" at the top where the relative CSR position is illustrated. The arrows indicate the direction the crane is moving to.

The orientation of the coordinate axes was retained. A delay in the change of the magnetic field can be observed for every component, as the magnetic field does not match for both moving directions. The correlation between the distance and the influence on magnetic field is conspicuous for component y and z. For both cases, still and moving, the crane seems to have a maximal influence on the magnetic field at the CSR of about ≈ 1 µT.

Injection Line

Figure 6.8: Injection line leading the beam into the CSR visible on the right side. The black boxes protect the laser used for photo-detaching.

Moreover the magnetic field at the injection line (Fig. 6.8) was measured. Measurements were contained to the section, starting at the 90°-deflector, where both platform beam lines encounter, and ending at the CSR casing. The electromagnetic coils around the photodetachment section were turned off while measuring. As before, measurements were taken at four positions around the beam line in order to estimate the field strength at the ion beam. Without a CSR casing measurement position can be chosen to be close to the beam line. Measurements were positioned at each corner around the vacuum tube: left-up, left-bottom, right-up and right-bottom. Usually 4.5 cm above or beneath the ion beam and 4.5 cm right or left of the beam. Only at the boxes protecting the laser this could not be accomplished. There, measurement positions were 40 cm beside the ion beam. The top positions were located 20 cm above the beam and the bottom ones 25 cm underneath it. All 4 corner measurements were averaged in Fig. 6.9. Compared to the CSR the ab-

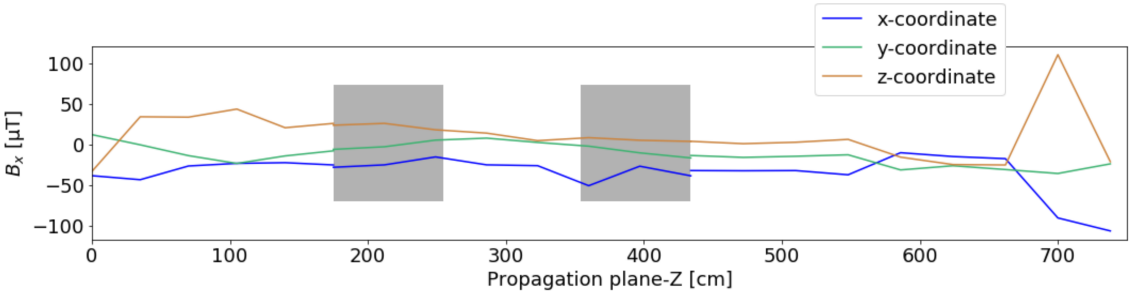

Figure 6.9: Magnetic field measured in the injection section. Measurements range from the 90°-deflector (0 cm), where both platform beam lines encounter, to the CSR casing (740 cm). Grey boxes indicate the positions of both laser boxes.

solute magnetic field 47 µT ± 27 µT is stronger and fluctuates significantly more. On the one hand this can be attributed to manufactured material of the injection line, where less attention was paid on its non-magnetic quality. On the other hand a large iron pillar close to the beam line disturbs its surroundings. It can be seen in Fig. 6.8 between both laser boxes, coloured in black. The peak at 700 cm originates from a pressure gauge. The discontinuities at the laser box boundaries arise from double measurements taken at the same location at the propagation plane, but once close to the beam line and once more at larger distances determined by the laser box geometry.

7 Compensating the Earth's Magnetic Field

The magnetic field inside the CSR, caused from the external earth's field, should be compensated by installing electromagnetic coils around the CSR. Fig. 7.1 features one possibility to structure those coils. Is was distinguished between long sections at the merged beams and diagnostics section and short ones at the e-cool and opposite side. Coils are intended to be attached outside at the CSR casing. As only field components perpendicular to the ion beam shall be compensated, resulting in 2 coil pairs per section. At the CSR corners the beam is not aligned parallel to the straight sections, thus compensation works only partly there. Taking the x-component as an example, optimal compensation at one straight section is achieved when

$$\int B_x^{Coils} dS = \int B_x^{Earth} dS, \tag{7.1}$$

where B_x^{Coils} denotes the x-component of the magnetic field induced by the coils along the line S and B_x^{Earth} denotes the x-component of the earth's magnetic field

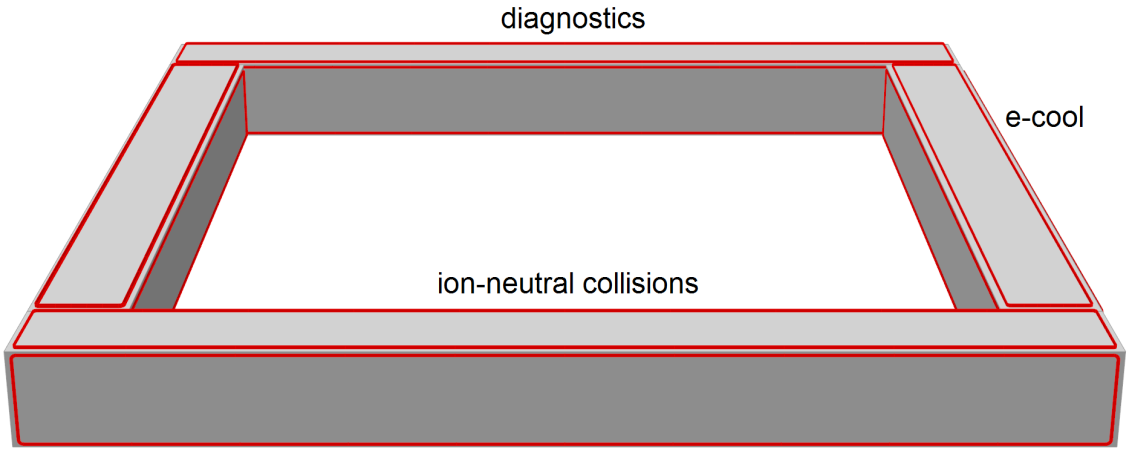

Figure 7.1: Schematic proposal for electro magnetic coil installation (red) around the CSR in order to compensate for the external magnetic field.

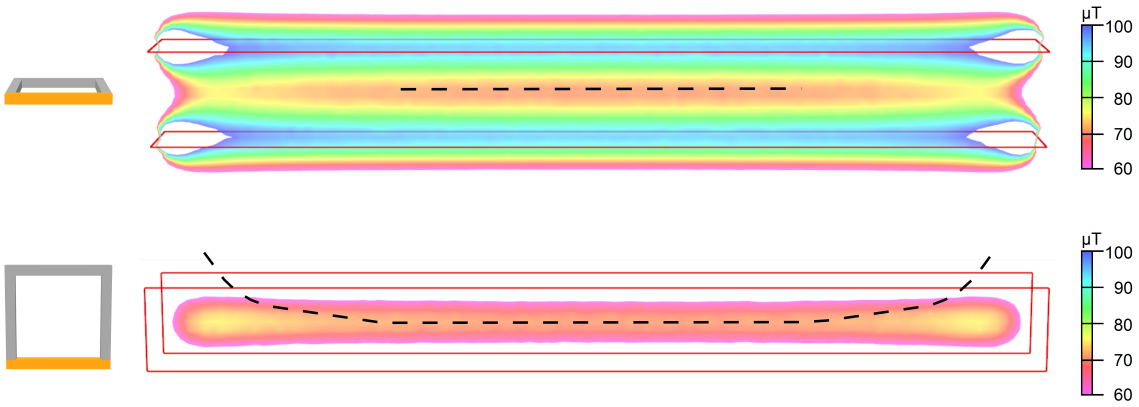

Figure 7.3: Magnetic field maps of a coil pair installed on top and underneath the CSR. The vertical field component is displayed in two different planes illustrated in the CSR images on the left. The coils have a length of 10.64 m, the width amounts to 1 m and have a distance of 1.1 m to each other. The long parts of the simulated coils compensating the horizontal component a positioned alike. The dashed line indicates the position of the ion beam, which is shifted vertically upwards by 5 cm. The magnetic field corresponds to an electromagnetic coil with 100 turns applied to a current of 1 Ampere.

measured in chapter 6. The path S was chosen to be along the points from Fig. 6.9, in order to compensate for the external field calculated there. Thus, compensation is adjusted along the straight CSR sections and will deviate from the desired ion beam position at the CSR corners. In order to estimate the magnetic field induced by the coils the finite element software Opera-3d was used. Its Static Electromagnetics Module, formerly called TOSCA, can calculate magneto- and electrostatic fields and DC current flows.

Fig. 7.3 shows the magnetic field of the same pair of coils. It depict only the vertical magnetic field component, but varying vertically in the upper panel and horizontally in the bottom one. The spatial orientation of the coils at the CSR is marked in yellow at the images on the left. At the center region deviations from perfect ion beam trajectory lead horizontally to an decreasing magnetic field and vertically to an increasing one. Besides, it can be seen that the ion beam leaves the center between the coil at both ends of the coils. Therewith it also leaves the part of the most homogeneous field. This is of special interest since the magnetic field was compensated only to be at a minimum at the center of the CSR casing.

Utilizing Eq. 7, Opera-3d predicts currents up to 55 Ampere, summarized over all coil turns, in order to compensate the external field properly. Fig. 7.4 depicts

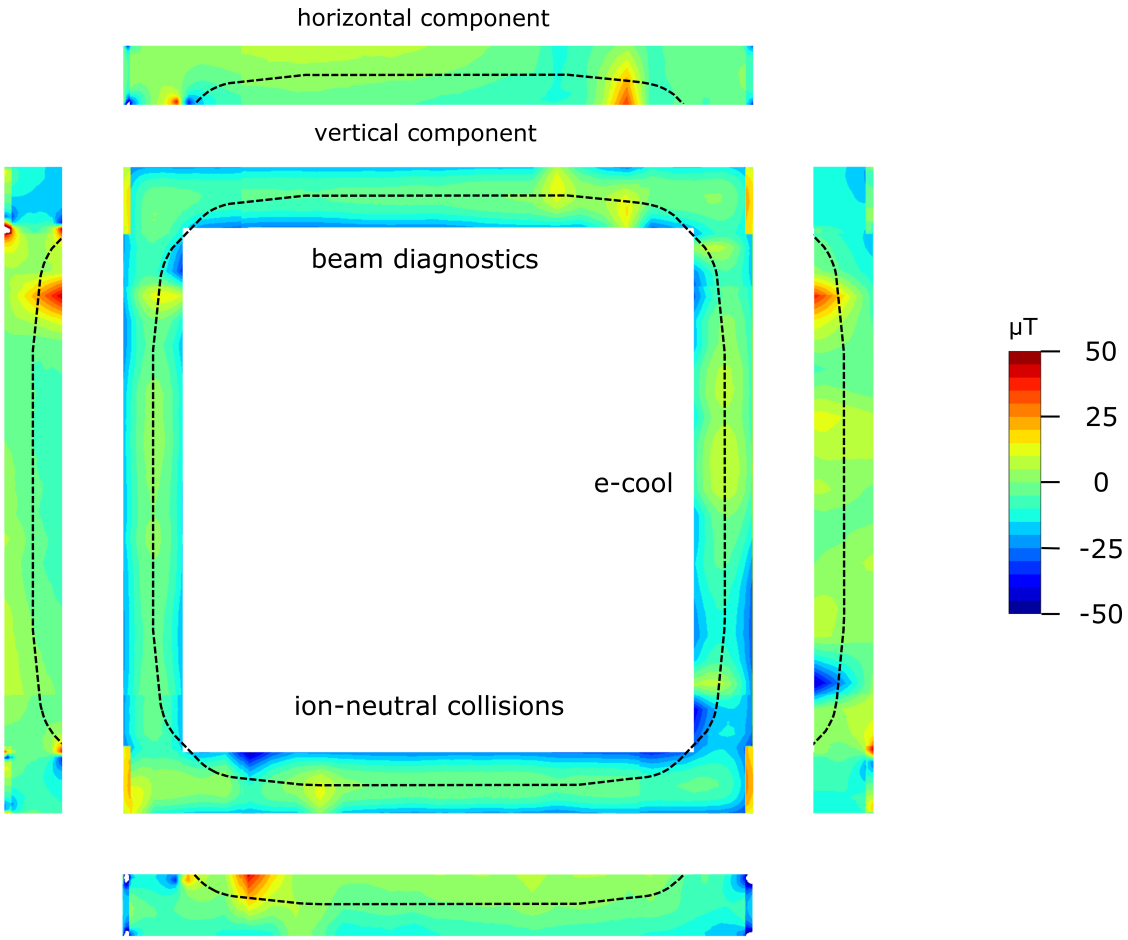

Figure 7.4: Superposition of the measured external field and the compensation field of electromagnetic coils. Positive field values indicate fields toward the direction of observation for the vertical components, and fields towards the top and right of the picture for horizontal components. The dashed lines denotes the trajectory of the stored ion beam.

the superposition of of the measured external field and the compensation field of electromagnetic coils. Mostly the ion beam, marked with a dashed line, is located at regions where the magnetic field is compensated almost to zero, indicated with green color. Pressure gauges close to the corners give rise to artefacts exhibiting strong field magnitudes. Moreover, the field becomes inhomogeneous at positions where the beam leaves the center region of the coils. It should be noted that the beam crosses territory at the edges where no magnetic field was surveyed. Observing the magnetic field close by, it can be assumed that the coils have a negative effect there. The tail of the short coils have a negative effect, too. This can be seen in the horizontal component at the point where the beam enters the ion neutral

section. The upended rectangles at each corners with exceptional high magnetic field strengths are artefacts, caused from non surveyed areas. Investigating the same positions as in Fig. 6.4 yields a mean magnetic field strength 0 T for components vertical to the straight sections, with a mean magnetic field amplitude of 4 µT ± 7 µT.

Fig. 7.5 depicts the properties of ion-neutral collisions for a cooled ion beam. It is influenced by an external magnetic field and the field of the coils compensating it. The ion beam appears straight, only being perturbed at the vertical deflectors and quadrupoles. Again, the main peak, the bump to higher energies and the high energy tail can be related to the center drift section, the quadrupole doublets and 6°-deflectors, respectively. The Maxwell-Boltzmann fit yields the best bet for achievable collision energies at the CSR using H_3^+ at 51 keV and C at 202,7 keV. As the fit describes mainly the main peak the collision energy T = 64 K should not be taken as a realistic thermal value, but as an estimate of the lowest collision energies achievable when the full velocity distribution is taken into account. It is obvious from the graph that a thermal distribution is no longer a good approximation, even for the low-energy part of the spectrum.

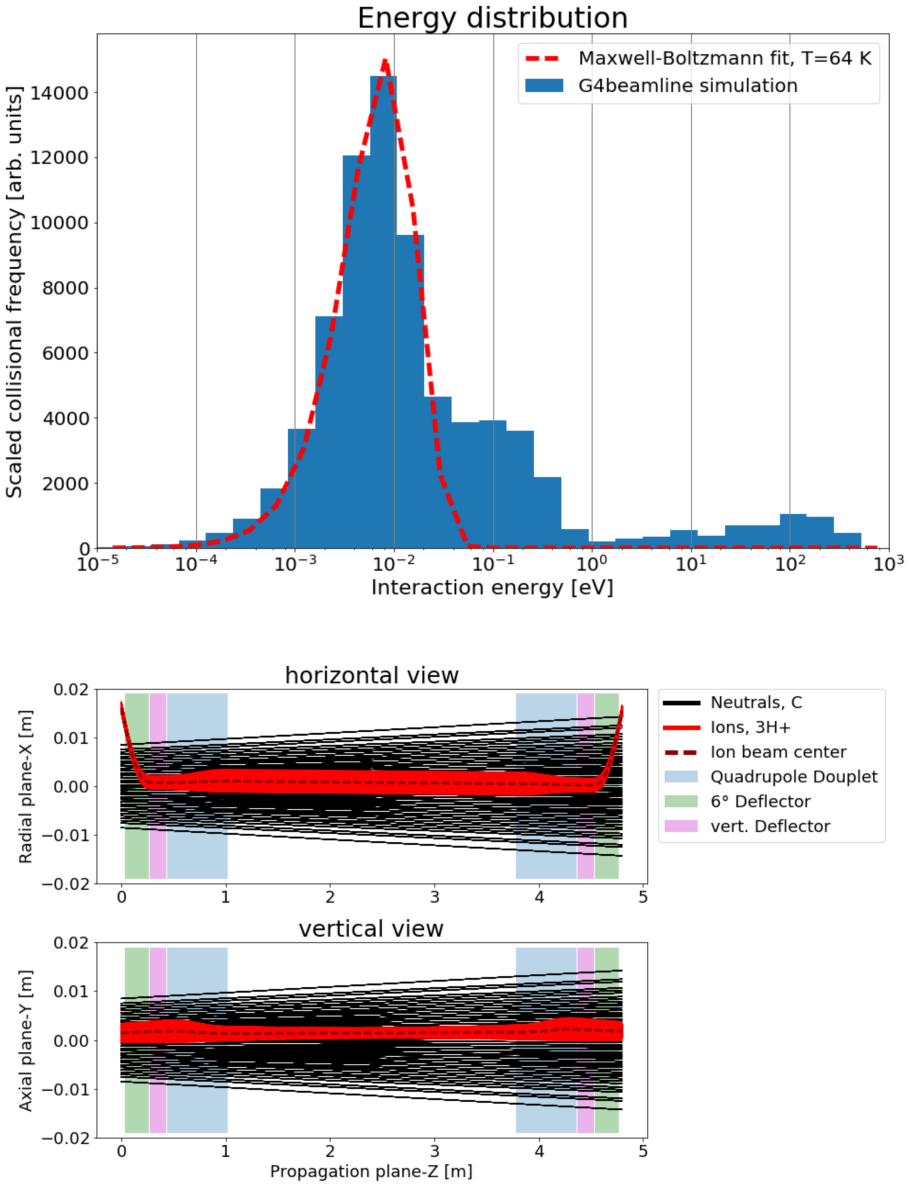

Figure 7.5: Properties of ion-neutral collisions for a cooled ion beam (corresponding to 2% CSR acceptance) influenced by an external magnetic field and the compensation from individual coils at each section.

8 Summary

Reactions between ions and neutral species are pivotal for gas-phase chemistry in interstellar clouds, where they represent approximately 2/3 of all reactions [30]. However, only a few rate coefficients have been measured under astrophysical temperatures, leading to wrong models of the chemical network. The merged beams experiment, housed at the Cryogenic Storage Ring (CSR), is capable of investigating these coefficients under proper conditions.

In order to evaluate if the collision temperature in the experiment matches the astrophysical cloud temperatures 10-100 K, simulations were done. The H_3^+ ion beam was simulated in G4beamline and the C neutral beam with Python, using a geometric approach.

Gathering slit-wise all possible reactions at the collision area allows to calculate the relative collision energy distribution in a non-relativistic limit. The distribution consists of a main peak from collisions at the drift section and shows features from the quadrupole doublets, 6°-deflectors and steerer to higher energies. A Maxwell-Boltzmann distribution, fitted to the main peak, provided information about the lowest accessible collisions temperature. Taking the best case scenario with a point-like ion beam and no influence of an external magnetic field on the ion beam, collision temperatures of 9 K seem accomplishable. The ion beam emittance remains a problem, since it is unknown, but can affect the ion-neutral collision temperatures up to 200 K. However, the main difficulties emerge from the earth's magnetic field, which increases the collision temperature almost by 600 K, even when its assumed to be fully homogeneous.

With the magnetic field having a massive impact on the stored ion beam a precise investigation is necessary. Since the beam location itself is inaccessible, a series of over 400 measurements was taken around the CSR casing. A distance weighted mean at the ion beam positions yields a magnetic field strength of 39 µT ± 8 µT. It was primarily disturbed by pressure gauges installed under the ring, which possess magnets themselves. It should be noted, that influence range measurements of the p-gauges were taken outside of the ring. They predict no influence of the ion beam.

However, the CSR casing prevents confirmation.
Another device, actually disturbing the magnetic field in the whole experimenting hall, is the crane. Different crane positions were investigated for a moving and a resting crane. Movement shows a delay in the magnetic field appearance, but the same amplitude of ~ 1 µT.
Furthermore the magnetic field along the injection line to the CSR was measured. Compared to the CSR the magnetic field 47 µT $\pm$ 27 µT is stronger and fluctuates significantly more. Presumably this can be attributed to the manufactured material, where minor attention was paid on its non-magnetic quality.
In order to compensate for the external magnetic field electromagnetic coils will be installed around the storage ring. With the configuration of two long and two short coil sections around the CSR, Opera-3d simulations predict a decrease of the perpendicular component of the magnetic field to 4 µT $\pm$ 7 µT , while being zero in the mean along chosen lines. Difficulties emerge especially at the CSR corners, where the ion beam traverses the fringe fields of the coils. Moreover, a coil width of 1 m leads to uncovered parts of the ion beam trajectory, where the coils even have a negative effect in the magnetic field. Additionally, the usage of short coils, which end immediately before the CSR corner lead to turbulences directly at the ion beam trajectory. However, the usage of such coils promises a decrease of collision temperature as low as 64 K.

9 Bibliography

[1] The cologne database for molecular spectroscopy. http://www.cdms.de/. Online; accessed 8 May 2017.

[2] G. L. Pilbratt, J. R. Riedinger, T. Passvogel, G. Crone, D. Doyle, U. Gageur, A. M. Heras, C. Jewell, L. Metcalfe, S. Ott, and M. Schmidt. Herschel Space Observatory. An ESA facility for far-infrared and submillimetre astronomy. *A&A*, 518:L1, July 2010.

[3] R. D. Gehrz, T. L. Roellig, M. W. Werner, G. G. Fazio, J. R. Houck, F. J. Low, G. H. Rieke, B. T. Soifer, D. A. Levine, and E. A. Romana. The NASA Spitzer Space Telescope. *Review of Scientific Instruments*, 78(1):011302–011302, January 2007.

[4] E. T. Young, E. E. Becklin, P. M. Marcum, T. L. Roellig, J. M. De Buizer, T. L. Herter, R. Güsten, E. W. Dunham, P. Temi, B.-G. Andersson, D. Backman, M. Burgdorf, L. J. Caroff, S. C. Casey, J. A. Davidson, E. F. Erickson, R. D. Gehrz, D. A. Harper, P. M. Harvey, L. A. Helton, S. D. Horner, C. D. Howard, R. Klein, A. Krabbe, I. S. McLean, A. W. Meyer, J. W. Miles, M. R. Morris, W. T. Reach, J. Rho, M. J. Richter, H.-P. Roeser, G. Sandell, R. Sankrit, M. L. Savage, E. C. Smith, R. Y. Shuping, W. D. Vacca, J. E. Vaillancourt, J. Wolf, and H. Zinnecker. Early Science with SOFIA, the Stratospheric Observatory For Infrared Astronomy. *The Astrophysical Journal Letters*, 749:L17, April 2012.

[5] A. Wootten. Atacama Large Millimeter Array (ALMA). In J. M. Oschmann and L. M. Stepp, editors, *Large Ground-based Telescopes*, volume 4837 of *Proc. SPIE*, pages 110–118, February 2003.

[6] E. Herbst and W. Klemperer. The Formation and Depletion of Molecules in Dense Interstellar Clouds. *Astrophysical Journal*, 185:505–534, October 1973.

[7] E. E. Ferguson, F. C. Fehsenfeld, and A. L. Schmeltekopf. *Ion-Molecule Reaction Rates Measured in a Discharge Afterglow*, chapter 6, pages 83–91. 1969.

[8] N. G. Adams and D. Smith. The selected ion flow tube (SIFT); A technique for studying ion-neutral reactions. *International Journal of Mass Spectrometry and Ion Processes*, 21:349–359, October 1976.

[9] Frank Hinterberger. *Physik der Teilchenbeschleuniger und Ionenoptik*. Springer-Verlag, Berlin Heidelberg, 2 edition, 2008.

[10] F. Hinterberger. *Physik der Teilchenbeschleuniger und Ionenoptik*. Springer Berlin Heidelberg, 2013.

[11] Harald Mutschke Stephan Schlemmer, Thomas Giesen. *Laboratory Astrochemistry: From Molecules through Nanoparticles to Grains*. Wiley-VCH, 2014.

[12] F. A. Lindemann, Svante Arrhenius, Irving Langmuir, N. R. Dhar, J. Perrin, and W. C. McC. Lewis. Discussion on "the radiation theory of chemical action". *Trans. Faraday Soc.*, 17:598–606, 1922.

[13] George Gioumousis and D. P. Stevenson. Reactions of gaseous molecule ions with gaseous molecules. v. theory. *The Journal of Chemical Physics*, 29(2):294–299, 1958.

[14] R. von Hahn, A. Becker, F. Berg, K. Blaum, C. Breitenfeldt, H. Fadil, F. Fellenberger, M. Froese, S. George, J. Göck, M. Grieser, F. Grussie, E. A. Guerin, O. Heber, P. Herwig, J. Karthein, C. Krantz, H. Kreckel, M. Lange, F. Laux, S. Lohmann, S. Menk, C. Meyer, P. M. Mishra, O. Novotný, A. P. O'Connor, D. A. Orlov, M. L. Rappaport, R. Repnow, S. Saurabh, S. Schippers, C. D. Schröter, D. Schwalm, L. Schweikhard, T. Sieber, A. Shornikov, K. Spruck, S. Sunil Kumar, J. Ullrich, X. Urbain, S. Vogel, P. Wilhelm, A. Wolf, and D. Zajfman. The cryogenic storage ring CSR. *Review of Scientific Instruments*, 87(6):063115, June 2016.

[15] Andrey Shornikov. An electron cooler for ultra-low energy cryogenic operation. PhD thesis, Ruprecht-Karls-Universität, Heidelberg, Germany, 2012.

[16] Stephen Vogel. Developments at an electrostatic cryogenic storage ring for electron-cooled kev energy ion beams. PhD thesis, Ruprecht-Karls-Universität, Heidelberg, Germany, 2016.

[17] Felix Laux. Entwicklung von kapazitiven positions-, strom und schottkysinalmesssystemen für den kryogenen speichering csr. PhD thesis, Ruprecht-Karls-Universität, Heidelberg, Germany, 2011.

[18] M. Grieser M. Lange F. Laux Tobias Sorg R. von Hahn T. Sieber, K. Blaum and A. Wolf. Beam diagnostics for the prototype of the cryogenic storage ring csr. In proceedings of EPAC2008, pages 1287-1289, Genoa, Italy, 2008.

[19] J Ullrich, R Moshammer, A Dorn, R Dörner, L Ph H Schmidt, and H Schmidt-Böcking. Recoil-ion and electron momentum spectroscopy: reaction-microscopes. *Reports on Progress in Physics*, 66(9):1463, 2003.

[20] R. Moshammer, M. Unverzagt, W. Schmitt, J. Ullrich, and H. Schmidt-Böcking. A 4 recoil-ion electron momentum analyzer: a high-resolution "microscope" for the investigation of the dynamics of atomic, molecular and nuclear reactions. *Nuclear Instruments and Methods in Physics Research Section B: Beam Interactions with Materials and Atoms*, 108(4):425 – 445, 1996.

[21] H.Grote and C.Iselin. MAD 8 - Methodical Accelerator Design. CERN.

[22] Opera-3d reference manual. Vector Fields Limited, 24 Bankside, Kidlington, Oxford OX5 1JE, England, 1996.

[23] Florian Grussie. Experimental sudies of ion-neutral reactions under astrophysical conditions. PhD thesis, Ruprecht-Karls-Universität, Heidelberg, Germany, 2016.

[24] G4beamline. http://g4beamline.muonsinc.com. Online; accessed 27 June 2017.

[25] Geant4. http://geant4.cern.ch. Online; accessed 23 June 2017.

[26] H. Bruhns, H. Kreckel, K. A. Miller, X. Urbain, and D. W. Savin. Absolute energy-resolved measurements of the $h^- + H \rightarrow h_2 + e^-$ associative detachment reaction using a merged-beam apparatus. *Phys. Rev. A*, 82:042708, Oct 2010.

[27] R A Phaneuf, C C Havener, G H Dunn, and A Müller. Merged-beams experiments in atomic and molecular physics. *Reports on Progress in Physics*, 62(7):1143, 1999.

[28] Harald J.W Müller-Kirsten. *Basics of Statistical Physics*. World Scientific, 2. edition, 2013.

[29] Projekt elektronik. http://www.projekt-elektronik.de/as-u3d-geo-x-300px/. Online; accessed 13 December 2017.

[30] J. Woodall, M. Agúndez, A. J. Markwick-Kemper, and T. J. Millar. The UMIST database for astrochemistry 2006. *A&A*, 466:1197–1204, May 2007.

Erklärung:

Ich versichere, dass ich diese Arbeit selbstständig verfasst habe und keine anderen als die angegebenen Quellen und Hilfsmittel benutzt habe.

Heidelberg, den (Datum) .....

Danksagung

An dieser Stelle möchte ich mich bei allen bedanken, die mich im letzten Jahr begleitet haben:
Holger Kreckel für die Möglichkeit eine Masterarbeit bei ihm anzufertigen. Ich habe den Freiraum und das selbstständige Arbeiten genossen, wobei es äußerst angenehm war zu wissen, dass er sich immer Zeit für Fragen und ausführliche Erklärungen nehmen wird.
Robert Moshammer für die freundliche und unverzügliche Übernahme des Zweitgutachters.
Manfred Grieser, der immer eine offne Tür für Fragen hatte und sich für Diskussionen immer Zeit genommen hat.
Florian Grussie für die experimentelle Einarbeit und die Möglichkeit an der Konstruktion des CSR teilzuhaben.
Florian Kerein für seine Unterstützung bei der Aufnahme von zahlreichen Messreihen.
Sunny Saurabh for being a pleasant and helpful office member.
Chris Popp für viele als auch konstruktive Anregungen beim korrigieren meiner Arbeit.
Dem gesamten CSR Team für eine sehr angenehme Arbeitsatmosphäre.
Meiner Familie für ihre Unterstützung.
Meiner Freundin Hannah für den Rückhalt den du mir fortwährend geboten hast.